Fall 12-5-2019

GROWTH AND CHARACTERIZATION OF ORGANIC FERROELECTRIC AND MAGNETIC THIN FILMS

Xuanyuan Jiang
University of Nebraska - Lincoln, yuanyuan@huskers.unl.edu

GROWTH AND CHARACTERIZATION OF ORGANIC FERROELECTRIC AND MAGNETIC THIN FILMS

by

Xuanyuan Jiang

A DISSERTATION

Presented to the Faculty of

The Graduate College at the University of Nebraska

In Partial Fulfillment of Requirements

For the Degree of Doctor of Philosophy

Major: Physics and Astronomy

Under the Supervision of Professor Xiaoshan Xu

Lincoln, Nebraska

December, 2019

GROWTH AND CHARACTERIZATION OF ORGANIC FERROELECTRIC AND MAGNETIC THIN FILMS

Xuanyuan Jiang, Ph. D.

University of Nebraska, 2019

Advisor: Xiaoshan Xu

Compared to inorganic materials, organic materials are environmentally friendly, flexible, and often with low cost. Inspired by these advantages, organic materials-based electronics have been intensively studied for comparable or better functionalities to inorganic electronics.

This dissertation mainly focuses on the growth and characterizations of organic ferroelectrics and magnetic thin films. For organic ferroelectrics, we investigate the growth and ferroelectric measurements of thin film croconic acid (CA), a proton-transfer molecular ferroelectric (FE) material with a large spontaneous polarization and a small coercive field, as well as the origin of ferroelectricity in CA in terms of the photostriction effect, including the discovery and explanation of an abnormal long relaxation time. For organic magnetic materials, we focus on a spin crossover (SCO) complex, [Fe{H2B(pz)2}2(bipy)] (BIPY) with high spin (HS) and low spin (LS) states, which can be switched by photoexcitation, pressure, magnetic or electric field. This dissertation mainly explains the interface effect on the spin state transition of BIPY complex. Finally, we fabricate organic multiferroic thin film device by depositing the ferroelectric CA and SCO BIPY on the interdigital bottom electrodes and realize the isothermal resistive switching.

To my parents, my fiancée and my friends

Preface

Compared to inorganic materials, organic materials are environmentally friendly, flexible, and often with low cost. Inspired by these advantages, organic materials-based electronics have been intensively studied for comparable or better functionalities to inorganic electronics.

During my PhD study, I've been focusing on the exploration and investigation of ferroelectric and magnetic molecular organic materials. Furthermore, to diminish the device size and enhance interface effects, we are aiming for the organic functional thin films. This thesis covers two types of organic materials, ferroelectric Croconic Acid (CA) and paramagnetic $[Fe\{H_2B(pz)_2\}_2(bipy)]$ (BIPY).

CA is a single-component proton-transfer ferroelectric material with small molecular size. It has large spontaneous polarization, small switching field, and strong structure-property coupling. It is a good candidate to replace inorganic ferroelectric materials. The spin crossover molecular complex BIPY can switch between two spin states, by various external stimuli. The molecular structure, electronic structure, and charge transport properties are coupled to the spin states, which offer multiple write-read modes. The study of this complex will boost the development of molecular devices.

Chapter 1 and 2 introduce background knowledge and information on the methods that are employed in my projects.

Chapter 3 discusses the growth conditions for CA thin film, which includes full coverage on the substrate, small surface roughness and good crystallization. This study indicates the potential of substituting inorganic ferroelectric materials by organic ferroelectric CA.

Chapter 4 investigates the photostriction effect in CA. Ultralong relaxation time after photoexcitation has been observed. This abnormal effect makes CA a promising optoelectronic material.

Chapter 5 discusses the effects of interface on the spin transition of BIPY. The enhanced cooperative effect and coordination effect triggered the coexistence of two spin states over a wide temperature range.

Chapter 6 combines the CA and BIPY in an in-plane device. Upon the polarization reversal in CA, the resistance state in BIPY changes. The nonvolatile resistive switching is achieved in the organic multiferroic junction.

Chapter 7 summaries all my work during my Ph.D. study.

Acknowledgements

I would like to express my foremost and sincere feeling of gratitude to my advisor Prof. Xiaoshan Xu. He is knowledgeable, insightful and professional, who dedicates himself to both science and education. I really appreciate those opportunities he provided to me, to work on the top-class instruments in our laboratory and the national laboratories, to attend conferences and meet people all over the world, to collaborate with people from other institutes, and most importantly, to work with and learn from him. He has taught me so much and helped me to gain deeper and better views of problems in physics, mathematics and programming. He has been supportive, open-minded, caring a lot about me and ready to help all the time, guiding and helping me to overcome the difficulties, not only in my projects but also in my daily life. His intelligence, professionalism and passion impressed me and inspired me to seek career in the fundamental science, to think independently, to be generous and careful to others. I would not be able to finish the program, become a better personal and professional, and figure out my lifetime goal without his selfless help.

I would also like to show my gratefulness to other supervisory committee members of mine. In particular, I want to thank Prof. Peter Dowben for offering me the chance to explore a brand-new research topic and collaborate with him and helping me to show the importance of my projects to the editors and referees and to look for postdoctoral positions.

I would thank Prof. Stephen Ducharme for the discussions on many physical problems and the guidance on the research directions, and Prof. Jian Zhang for the synthesis of high-quality organic materials.

I appreciate the help from Prof. Alexei Gruverman, Prof. Alex Enders, Dr. Anthony DiChiara, Dr. Alpha N'Diaye so much.

I would like to thank my collaborators, Dr. Xiao Wang, Dr. Haidong Lu, Pratyush Buragohain and Guanhua Hao, and our former and current group members, Dr. Yuewei Yin, Dr. Kishan Sinha, Dr.Xiaozhe Zhang, Dr. Yu Yun, Dr. Jing Li, Corbyn Mellinger, Yifan Yuan and Haohan Wang.

I want to express my sincere thanks to my parents, my fiancée Ming Li, and my friends for their love and support. My fiancée Ming helped me in every single academic step and supported me emotionally during my Ph.D. program.

Table of Contents

Chapter 1 Organic ferroelectrics and spin crossover complex

1.1 Organic ferroelectrics

1.1.1 Introduction of organic ferroelectric materials

Ferroelectric materials are promising for application in the electronic devices and memories due to their property of switching between two stable states by an external field. The fast switching, small device scale and relatively high operation temperature make ferroelectric material good candidates for the next generation of electronic devices[1–5]. The first organic ferroelectrics ever discovered (in 1920) was single crystal Rochelle salt. However, few organic ferroelectric material has been discovered after that. The past decade has seen discovery of a sequence of organic ferroelectrics by the structure analysis[6].

There are three types of organic ferroelectric materials, distinguished by different origins for their spontaneous polarization. The first type is based on dipolar molecules, shown in the Fig. 1.1.1 (a). For example, in Thiourea[6] and in the polymer Polyvinylidene fluoride (PVDF)[7], their single components (molecules) carry dipole moments. When these molecules are stacked in the unit cell without canceling all the dipole moments due to non-centrosymmetric crystal structure, the net polarization occurs.

The second type is the charge-transfer (CT) complex with electron donor-acceptor molecules. When the displacements are opposite for the donor and acceptor molecules, the dipole moments will be created, as seen in Fig. 1.1.1 (b). In tetrathiafulvalene-tetrachloro-p-benzoquinone (TTF-CA) crystals, the ferroelectric ordering comes from the so-called neutral-ionic (NI) phase transition, where the molecular-charge distribution will change when the electrons transfer from the donor to the acceptor molecules[8,9]. Another example is a 5,10-dihydro-5,10-dimethylphenazine-2,5-dimethyl-7,7,8,8-

tetracyanoquinodimethane (M2P-DMTCNQ) multicomponent system. The M2P molecule has two stable states: one neutral state with bent form and one ionized state with flat form. The molecule can transit from neutral state to the ionized state by accepting electrons transferring from the DMTCNQ molecule, accompanied by shape deformation. DMTCNQ is partially charged ($\rho \approx 0.5$) and flexible. During the charge transfer, the shape of the DMTCNQ molecule will change accordingly along with the M2P molecule. The shape deformation of the two molecules help to stabilize the charge transfer state, which generates the dipole moments in this two-component system[10].

The third type of organic ferroelectric materials is the hydrogen-bonded system[11,12,13]. In right figure of Fig. 1.1.1 (c), the hydrogen bonds connect the molecules in Hdabco$^+$. Since all the protons are attached to one side of the molecules, a net in-plane polarization is formed. By switching the position of protons in the hydrogen bonds, this in-plane polarization can be reversed.

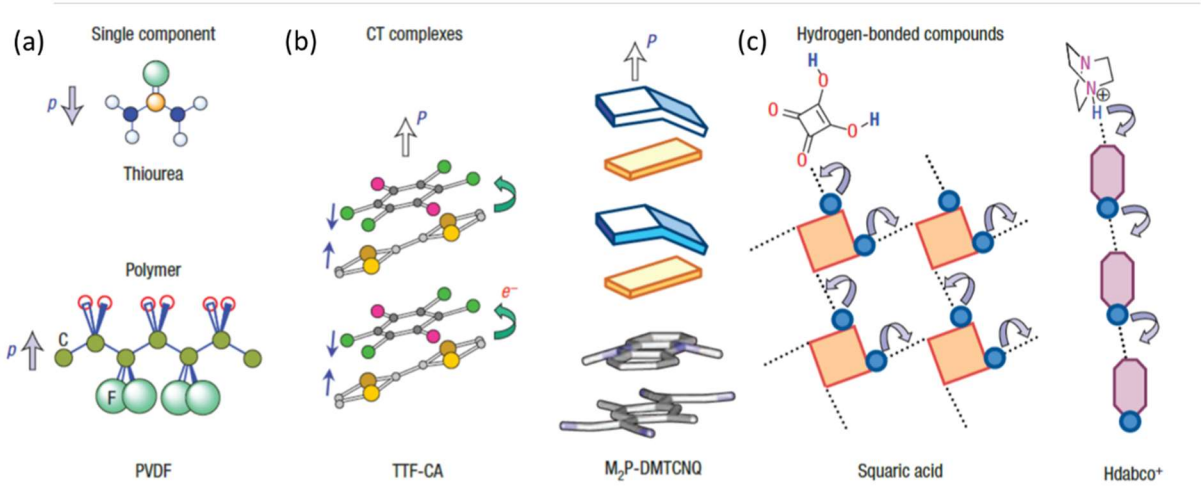

Fig. 1.1.1 Different origins of dipole moments in organic materials[6].

1.1.2 Phenomenological theory for ferroelectrics

One of the main physical properties of organic ferroelectric materials is the transition temperature from dielectric phase to ferroelectric phase. From the mean-field model[14], the temperature dependence of spontaneous polarization can be derived:

$$\langle p_i \rangle = \frac{p e^{\frac{pE_{eff}}{k_B T}} + (-p) e^{\frac{-pE_{eff}}{k_B T}}}{e^{\frac{pE_{eff}}{k_B T}} + e^{\frac{-pE_{eff}}{k_B T}}} \qquad \text{Eq. 1.1.1}$$

Here the net polarization $P = \frac{\sum p_i}{V} = \frac{\langle p_i \rangle}{v}$, p_i is dipole moment of molecules, V is total volume, v is the unit cell volume. And $E_{eff} = E + \chi P = \varepsilon P$, E is electric field, χ is electric susceptibility, ε is dielectric constant. Take $\frac{pE_{eff}}{k_B T} = x$, then $P(T) = P(x) = \frac{p}{v} L(x)$, where $L(x)$ is the Langevin function (see Fig. 1.1.2).

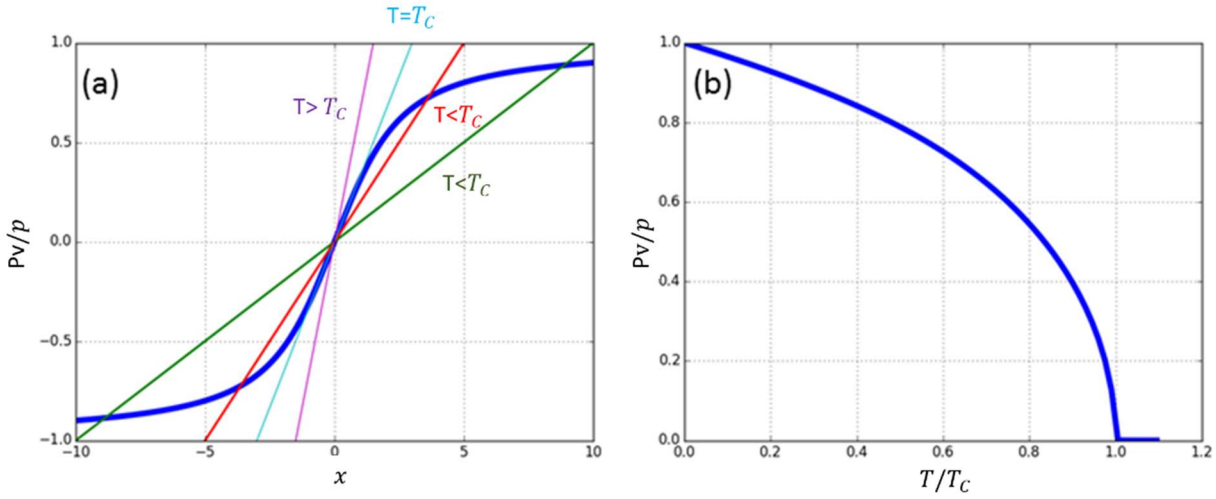

Fig. 1.1.2 (a) The plots of Langevin function and the linear function $P = \frac{k_B T}{\varepsilon p} x$, with different T. (b) The T dependence of spontaneous polarization P.

In Fig. 1.1.2 (a), the Langevin function and linear function $P = \frac{k_B T}{\varepsilon p} x$ are plotted. The solution of spontaneous polarization depends on the cross points between these two functions. When the temperature is much higher than the critical point T_C (the purple solid

line in Fig. 1.1.2 (a)), the slope of linear function is very large. The only cross point is when *P* equals zero. But when the temperature is lower than the critical point T_C (red and green solid lines), the slope is smaller, then there are nonzero cross points, which give nonzero spontaneous polarizations. By plotting these crossing points, we can get the temperature dependence of spontaneous polarization (Fig 1.1.2 (b)). When $T>T_C$, the P equals to zero; when $T<T_C$, the nonzero solutions of *P* exist; *P* saturates when $T<<T_C$.

The ferroelectric phase transition in this case is a second order phase transition, and we need to know the free energy change during this phase transition. According to Landau-Ginzburg-Devonshire (LGD) model[14, 15], the thermodynamic potential density can be described in this form:

$$\Phi = \Phi_0 + \alpha(T)\boldsymbol{P^2} + \frac{\beta(T)}{2}\boldsymbol{P^4} + \frac{\gamma(T)}{6}\boldsymbol{P^6} - \boldsymbol{EP} \qquad \text{Eq. 1.1.2}$$

where $\boldsymbol{E}$ is the electric field and the coefficients α, β, γ depend on temperature *T*. The free energy diagram with α<0 and zero electric field is plotted in Fig. 1.1.3 (a). For the second order phase transition, β should be positive. According to Ginzburg's assumption, when *T* is far from the phase transition temperature, $\alpha(T) = \alpha'_{T_C}(T - T_C), \beta = \beta_{T_C}$ and $\gamma(T) = 0$, where $\alpha'_{T_C} = (\frac{d\alpha}{dT})_{T=T_C} > 0$, T_C is the phase transition temperature. By minimizing the potential density without electric field, we can get the spontaneous polarization when $T < T_C$, $P_0^2 = -\frac{\alpha}{\beta} = \frac{\alpha'_{T_C}(T_C - T)}{\beta_{T_C}}$.

To obtain the relation between $\alpha(T)$ and dielectric constant $\varepsilon(T)$, we first take $\frac{\partial \Phi}{\partial P} = 0$, which gives $E = 2\alpha P + 2\beta P^3$. We then take small field approximation and reach $P = P_0 + (\frac{\partial P}{\partial E})_{P_0} E = P_0 + (\varepsilon - 1)\varepsilon_0 E \approx P_0 + \varepsilon\varepsilon_0 E$ when $\varepsilon \gg 1$. As a result, we can have

$$\frac{1}{\varepsilon_0 \varepsilon} = (\frac{\partial E}{\partial P})_{P_0} = 2\alpha + 6\beta P_0^2. \quad \text{Eq.1.1.3}$$

Note that for $T > T_C$, $P_0 = 0$; $T < T_C$, $P_0^2 = -\frac{\alpha}{\beta}$. Following Eq.1.1.3, the dielectric constant is

$$\varepsilon(T) = \begin{cases} \frac{1}{2\varepsilon_0 \alpha'_{T_C}(T-T_C)}, & T > T_C \\ -\frac{1}{4\varepsilon_0 \alpha'_{T_C}(T-T_C)}, & T < T_C \end{cases} \quad \text{Eq. 1.1.4}$$

When $T > T_C$, the system is in paraelectric phase, with zero spontaneous polarization. And when $T < T_C$, the system is in ferroelectric phase. The dielectric constant in paraelectric phase is twice as large as that in ferroelectric phase, as plotted in Fig. 1.1.3 (b).

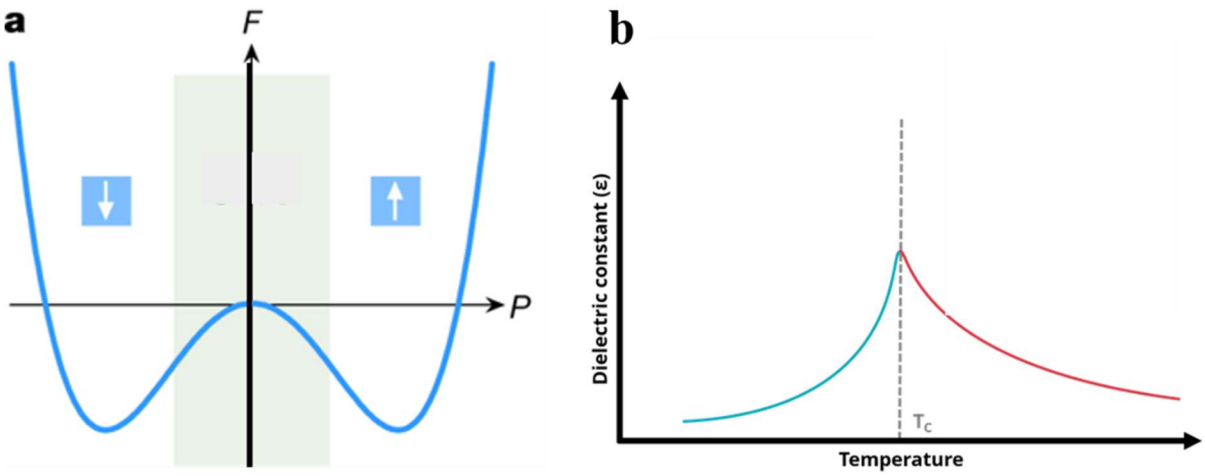

Fig. 1.1.3 (a) Landau free energy in ferroelectric materials. (b) The dielectric constant in both ferroelectric and paraelectric phases[36].

1.1.3 Ferroelectric Domains

Landau free energy describes at the atomic level how the dipole moments are aligned to give macroscopic polarization in infinite materials. In reality, we can always see different domain structures in ferroelectric thin films[16]. This makes us consider the reason of forming ferroelectric domains and how to decide the domain size.

Single crystal ferroelectrics have multidomain structures. The polarization is aligned within the domains; different domains hold different polarization directions. The polarizations in all domains sum up to zero net polarization, minimizing the total electrostatic energy. The domain size is determined by the competition between depolarization field energy and domain wall energies. For a finite ferroelectric domain, the polarization uniformity is broken at the domain boundary ($\nabla P \neq 0$), leading to the accumulation of bound charges. When the material is an insulator and exposed in vacuum, there are no screening charges that can be induced to compensate the bound charges. These uncompensated charges will produce the depolarization field E_{de}, and the energy associated to this depolarization field is $W_{de} = \frac{1}{2}\int_V D \cdot E_{de} dV$. Domain walls separate neighboring domains. If we take domain wall energy per unit area as σ, the total domain wall energy can be expressed as $W_w = \int_A \sigma dS$. Larger domain size leads to larger depolarization field energy and smaller domain wall energy since the wall area is smaller. So, to find the domain size, we need to calculate the minimum of $W_{de} + W_w$, both associated with domain shape.

An example of the 180° stripe domain structure in thin films is shown in Fig. 1.1.4, with film thickness *t*, domain width *d* ($d < t$), and total volume *V*. In this kind of structure, the depolarization energy can be calculated through $W_{de} = \iint \frac{\rho_1 \rho_2}{4\pi\varepsilon_0 r_{12}} d\tau_1 d\tau_2$, where ρ_1, ρ_2 are total charge densities in different volumes τ_1, τ_2, and $d\tau_1, d\tau_2$ are separated by r_{12}. The integral of 180° stripe domain gives us

$$W_{de} = \frac{\varepsilon^* d P_0^2 V}{t} \qquad \text{Eq. 1.1.5}$$

where ε^* is a constant that depends on dielectric constant and P_0 is the spontaneous polarization.

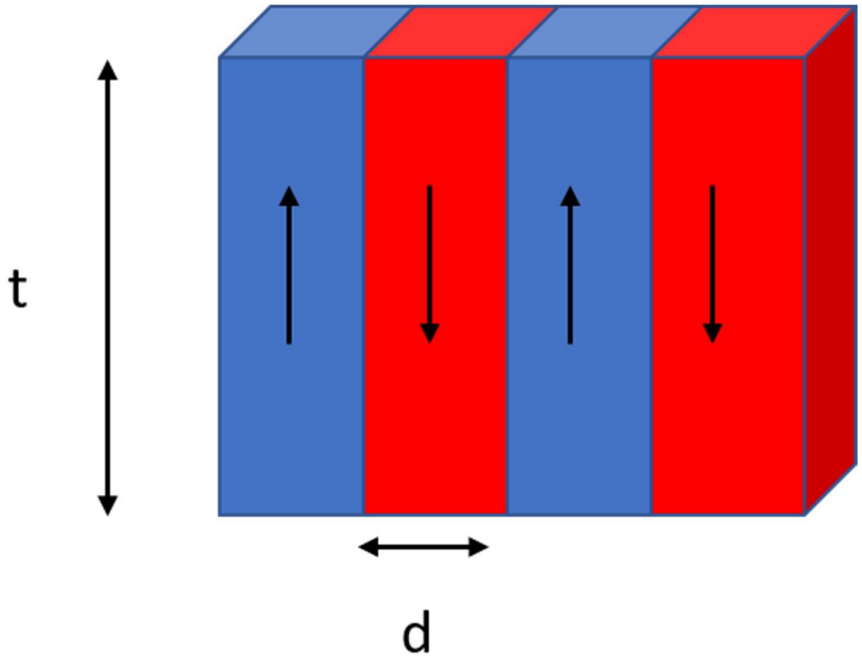

Fig. 1.1.4 The stripe domain structure with thickness *t* and domain width *d*.

The domain wall energy in this structure is simply $W_w = \frac{\sigma}{d}V$. Minimizing the sum of depolarization field and domain wall energies, we can get $d = (\frac{\sigma t}{\varepsilon^* P_0^2})^{1/2}$.

For semiellipsoid shaped domains as in figure 1.1.5, the depolarization energy is in the form[17]:

$$W_{de} = \frac{4}{3}\frac{\pi^2}{\varepsilon_a}P_0^2\frac{r^4}{l}\{-1 + \ln\left[\frac{2l}{r}\left(\frac{\varepsilon_c}{\varepsilon_a}\right)^{\frac{1}{2}}\right]\} \qquad \text{Eq.1.1.6}$$

And the domain wall energy is $W_w = \sigma\frac{\pi^2}{2}rl$. Again, the finite size of the semiellipsoid domain can be obtained by minimizing the total energy.

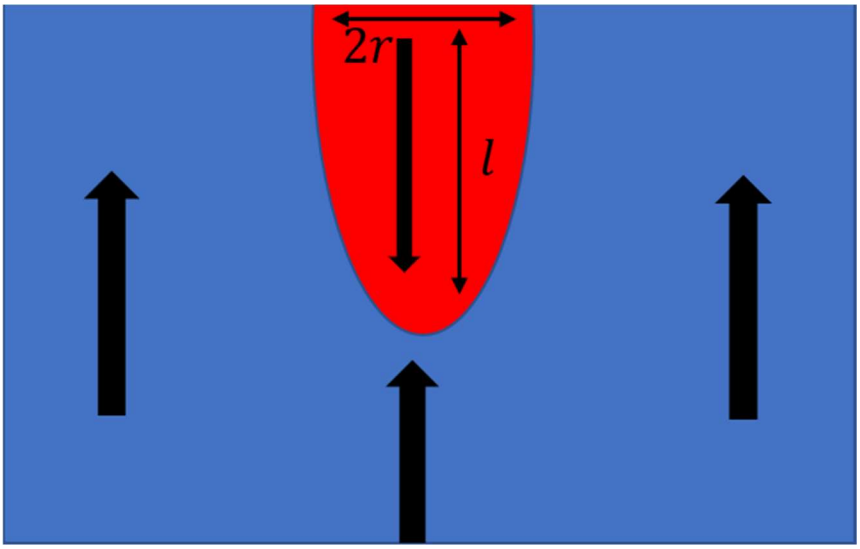

Fig. 1.1.5 A semiellipsoid domain with polarization pointing down. The semi-major axis is l and the semi-minor axis is r, $l \gg r$.

1.1.4 Polarization reversal

In ferroelectric materials, the spontaneous polarization can be switched by an external electric field. Basically, the polarization switching is due to the broken symmetry in Landau free energy induced by the external electric field. Without electric field, the states with $\pm P_0$ have the same free energies, both being global minima and stable. The energy barrier between these two states is determined by crystallography anisotropy, shape anisotropy and thermal fluctuation. To switch from one state to the other, the barrier needs to be overcome. Once the external electric field is applied, the symmetry of the energy profile is broken, and there remains only one global minimum, which represents the state with the polarization parallel with the external field. In a word, the polarization can align with external electric field, and if the electric field is reversed and has large enough magnitude, the polarization will be reversed.

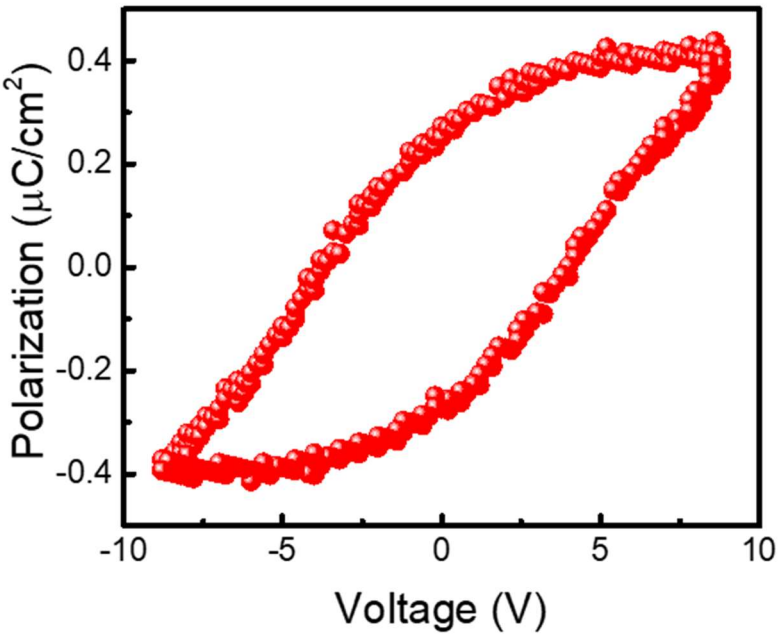

Fig. 1.1.6 The polarization hysteresis loop of 180 nm Croconic Acid thin film[27].

The sketch of polarization hysteresis loop by electric field is represented in Fig. 1.1.6. In this loop, the electric field needed for polarization switching is called coercive field E_C, and the remaining net polarization after the electric field is withdrawn is called remnant polarization P_r.

In an ideal case, the polarization will be switched instantly when the applied electric field is larger than the coercive field E_C. In reality, the polarization switching in ferroelectric materials takes time, which varies from μs to ms[18–21].The switching time depends on the microscopic structure, involving the domain wall dimensionality and atomic viscosity. And the switching field is not necessarily larger than the coercive field. It depends on the coercive field, depolarization field, domain wall energy, ferroelastic effect, piezoelectric effect, interface effect and defects.

There are two widely used polarization switching theories: one is called Kolmogorov-Avrami-Ishibashi (KAI) model[22], and the other one is the nucleation limited switching (NLS) model[20]. Both models assume that the polarization switching involves two aspects: nucleation of polarization reversal centers and domain growth of those nucleation centers.

The KAI model assumes that, under electric field, the nucleation centers form first, and then when those nucleation centers begin to grow, there is no new nucleation center created. The reversed domains will eventually expand to the whole sample. The switching time depends on the domain growth speed, which is related to the applied electric field. In KAI model, the polarization switching can be achieved even in a small electric field, as long as the nucleation centers can be formed. The centers can grow slowly under the small electric field and eventually cover the whole sample.

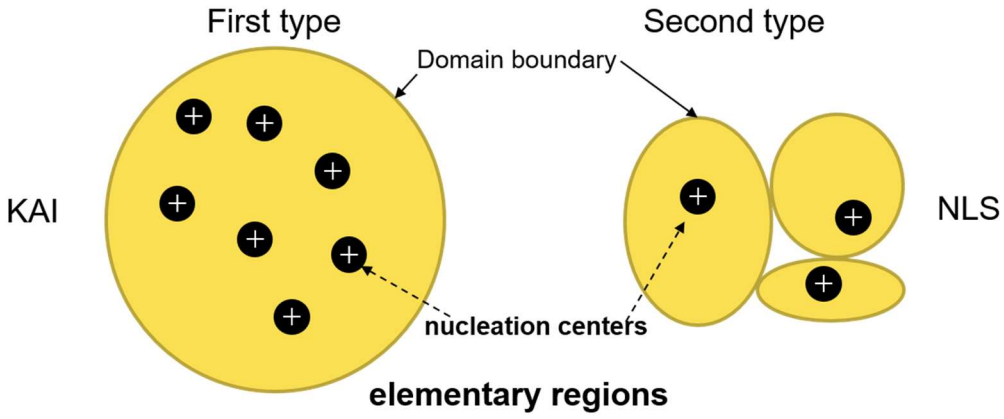

Fig. 1.1.7 Different nucleation process in KAI model and NLS model.

But in the NLS model, it's assumed that the activation energy to form nucleation centers is different in separated grains, and the domain growth of those centers is limited due to finite grain size, instead of expanding to the whole sample. So, in the NLS model, the polarization switching strongly depends on the electric field. Without large enough

electric field, nucleation centers will not be created in some grains, so the net polarization will not be fully switched. Fig .1.1.7 shows the difference between KAI model and NLS model.

Here we can quantitatively discuss the two models. In the KAI model, the polarization switching dynamics (see Fig. 1.1.8) can be expressed as:

$$\Delta P(t) = 2P_0\left(1 - \exp\left(-\frac{t}{t_0}\right)^d\right). \quad \text{Eq. 1.1.7}$$

Here $\Delta P(t)$ is the reversed polarization at different time, P_0 is the spontaneous polarization, t_0 is the time constant of domain growth and d is the domain wall dimensionality.

The time needed to completely switch the polarization in a single domain depends on the domain growth speed under electric field. At T=0 K, the domain growth speed v for different electric field E is:

$$v \propto \begin{cases} \exp\left(-\left(\frac{U_a}{k_B T}\right)\left(\frac{E_C}{E}\right)^{\mu}\right), E \ll E_C \\ (E - E_C)^{\theta}, E \geq E_C \\ E, E \gg E_C \end{cases} . \quad \text{Eq.1.1.8}$$

Here is U_a the activation energy, μ is dynamic parameter, and θ is related to dimensionality.

The KAI model was used to fit the time dependence of polarization switching during domain growth process under different electric field in a capacitor device, composed of 9 nm PVDF ferroelectric layer (fig. 1.1.8 a). And the electric field dependent domain growth speed in ferroelectric Pb(Zr,Ti)O_3 (PZT) thin films was studied using the KAI model in different temperature regions (fig. 1.1.8 b).

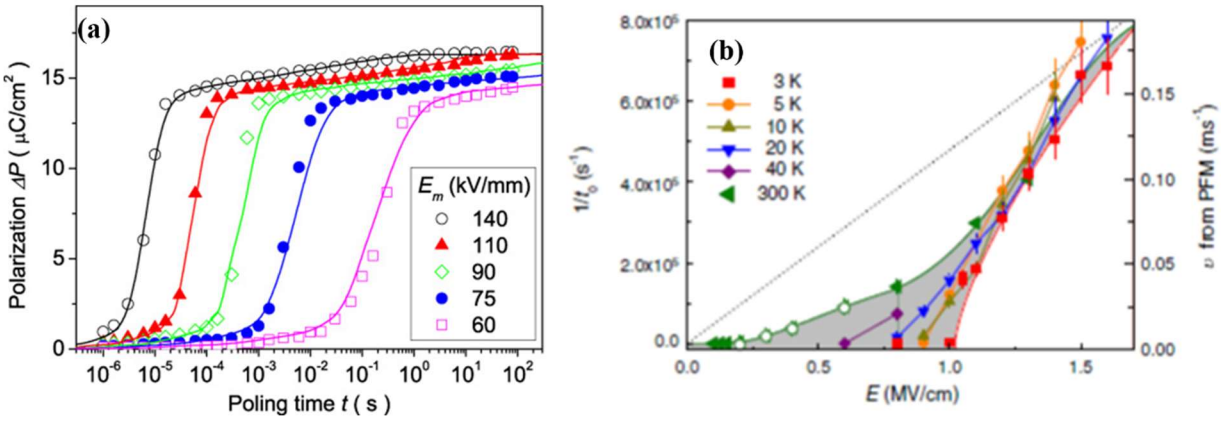

Fig. 1.1.8 (a) Fitting of the time dependence of polarization switching dynamics using KAI model[23].(b) The fitting of electric field dependence of domain growth speed for different temperature[23].

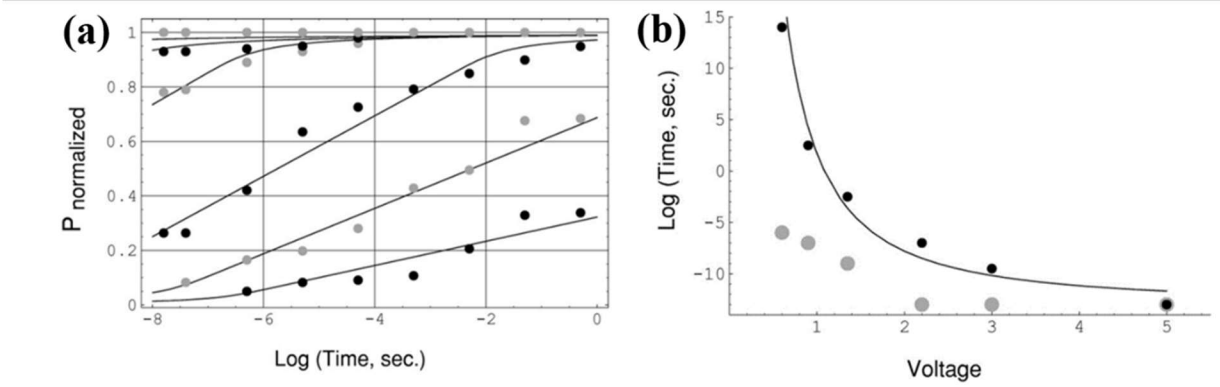

Fig. 1.1.9 (a) Fitting of time dependence of polarization switching under different electric field using NLS model, (b) Fitting of voltage dependence on switching time[20].

In NLS model, the time dependence of polarization switching (see Fig. 1.1.9) can be expressed as:

$$p(t) \propto \begin{cases} arctan\frac{lnt-l\ \ min}{\Gamma}, t < \tau_{min} \\ \frac{lnt-l\ \ min}{\Gamma}, \tau_{min} < t < \tau_{max} \\ \frac{ln\tau_{max}-ln\tau_{min}}{\Gamma} + arctan\frac{lnt-ln\tau_{max}}{\Gamma}, t > \tau_{max} \end{cases}, \qquad \text{Eq.1.1.9}$$

where $ln\tau_{max} \sim (\frac{V_0}{V})^d$.

The nucleation time is a distribution function. Between $\tau_{min}\ and\ \tau_{max}$ the probability is the same; beyond $\tau_{min}\ and\ \tau_{max}$, the probability will decay with a factor of Γ.

The domain switching behavior in PZT thin film was fit by NLS model in fig. 1.1.9 a; the voltage dependence of complete switching time was fit in fig. 1.1.9 b.

The two models need to be chosen carefully to describe different systems. The KAI model is normally used in single crystalline thin films, while the NLS model is widely used in polycrystalline ferroelectric materials.

1.1.5 Ferroelectricity in Croconic Acid

After we get the idea about main properties in ferroelectric materials, we can focus on one specific material that we are interested in, Croconic Acid (CA). The CA chemical form is $C_5H_2O_5$; its molecule is polar, as shown in Fig. 1.1.10 (a), with the positive and negative centers differing in positions. The molecules are connected by hydrogen bonds OH…O, and the hydrogen bonds forms a chain in molecules, which increases the total polarization. There are two independent types of hydrogen bonds chains (Fig. 1.1.10 (b)). One of the bonds is almost parallel with the *c* axis, causing a net polarization along *c* axis. The other bond zigzags along the c axis[24], which cancels the dipole moments along a and *b* axis and remains polarization along *c* axis. The combined hydrogen bond network stacks the molecules in a zigzag sheet, as illustrated in Fig. 1.1.10 (b). The crystal structure for CA is orthorhombic $Pca2_1$ (as shown in Fig. 1.1.10 (c)), without inversion symmetry. So, the net polarization remains nonzero.

Fig. 1.1.10 (d) shows the polarization and total energy change with the lattice distortion from centrosymmetric phase to non-centrosymmetric phase. The predicted

spontaneous polarization in CA single crystal is $P_s = 26\ \mu C\ cm^{-2}$, which is comparable to the polarization in $BaTiO_3$[26]. Fig. 1.1.10 (e) shows the intermolecular electronic structure.

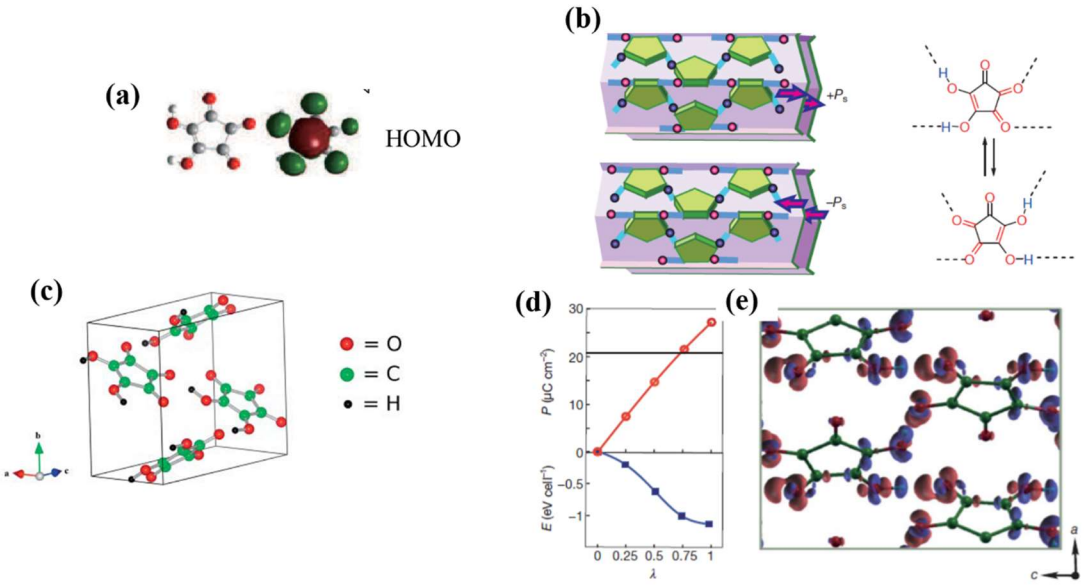

Fig. 1.1.10 (a) Atomic structure and electronic structure of CA molecule. (b) The two types of hydrogen bonds in zigzag crystal planes and the corresponding polarization switching due to the change in hydrogen bonds[24]. (c) The molecular stacking in a unit cell[25], (d) Polarization and free energy change with lattice distortion[24]. (e) Intermolecular electronic structure[24].

CA has many advantages, compared to other organic ferroelectric materials. The polarization switching in CA requires no rotation and flip of dipolar molecules, which needs to overcome large energy barrier from crystalline anisotropy. The switching in CA is governed by the change of the proton position in hydrogen bonds: by attaching proton atoms to the left side or right side of CA molecules, the polarization can be reversed. Since the energy barrier in hydrogen bonds is relatively low, the required switching external field

is small. The coercive field in CA single crystal is around 20 kV/cm with low frequency test[26].

Another good part of CA is that there is a large vertical projection of polarization when it is grown on the substrates. Due to its small molecular size and zigzag molecular stacking, the molecules grown on the substrates are not exactly lying down, so the hydrogen bonds between molecules can have out-of-plane projection. And due to the interface effect, the *c* axis of CA unit cell can point out-of-plane or tilt from in-plane direction, which gives the possibility of having out-of-plane polarization. This out-of-plane polarization in CA thin film was observed in our previous study[27]. All of these properties in CA, large polarization, small coercive field, existence of both vertical and lateral polarizations in thin film, make CA a very promising ferroelectric material, which can be widely used in ferroelectric tunneling junctions (FTJ) and other electronic devices.

1.2 Organic paramagnets - Spin crossover

1.2.1 Introduction

The molecular electronics is a trending topic in modern physics and engineering areas[28]. The concept of using a single molecule as the nanoscale memory device attracts much attentions. The coexistence of two spin states in spin crossover (SCO) complexes provides one path to achieve this goal. In these SCO complexes, the center of one molecule is composed by a transition-metal ion, which is surrounded by organic ligands. The spin state in the transition-metal ion depends on the ligand field, which can be switched by external stimuli, such as temperature, light, pressure, magnetic or electric field[29–33]. The change in spin states can be detected by the measurement of magnetic susceptibility,

electronic conductivity and local electronic structure. Here we take one SCO molecule [Fe{H2B(pz)2}2(bipy)] (BIPY) as an example to show the principles of the SCO complex.

1.2.2 Spin crossover complex BIPY

The molecule structure of BIPY is shown in Fig. 1.2.1 (a). The iron atom is surrounded by nitrogen atoms, forming six Fe-N bonds. Two states BIPY molecule, with different bond lengths/angles and spin configurations, have comparable energies. The state with four unpaired spins in 3d orbit is called the high spin (HS) state (S=2), and the state with all spins paired is called the low spin (LS) state (S=0).

The transition between these two states is determined by the competition between crystal field $\boldsymbol{W_{cry}}$ and spin-spin interaction $\boldsymbol{W_s}$. As shown in Fig. 1.2.1 (b), due to the six Fe-N bonds, the 3d electron energy level is split into two sublevels, e_g and t_{2g}. When the Fe-N bonds are short, the crystal field from nearby N ions to the center Fe ion is large. So, the e_g-t_{2g} energy splitting is increased. To minimize the total energy, all electrons fill the lower level t_{2g}, leading to S=0. On the other hand, when the Fe-N bonds are long, the crystal field is smaller, making the energy splitting smaller. In this case, to minimize the total energy, the electrons form maximum total spin (S = 2) based on the Hund's rules.

The transition temperature can be predicted using Fig. 1.2.1 (c). By plotting the Gibbs free energy $\boldsymbol{G = U + PV - TS}$ in HS and LS states, with $\boldsymbol{S_{HS} > S_{LS}}$ and $\boldsymbol{V_{HS} > V_{LS}}$, the two lines will have a cross point $\boldsymbol{T_C}$, below which the BIPY is more stable in LS state, otherwise HS state is more stable. The switching between the two spin states depends on the energy barrier in between (see Fig. 1.2.1 (d)), which is related to the intermolecular cooperative effect and substrate coordination effect. In chapter 6, we will discuss the interface effect on the spin state transition of SCO complex.

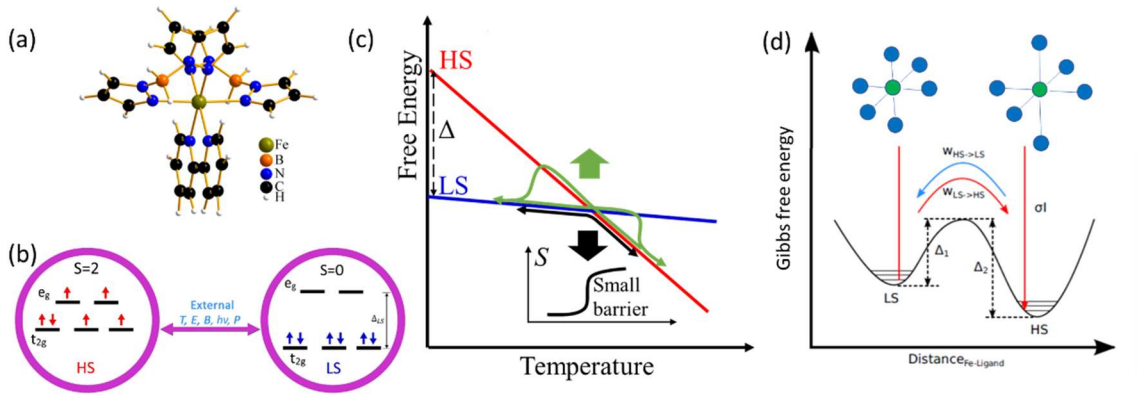

Fig. 1.2.1 (a) BIPY molecular structure. (b) Schematic plot of HS and LS states[34]. (c) Plot of enthalpy as a function of temperature for HS and LS states[35]. (d) Energy barrier between HS and LS states[28].

1.3 Reference

[1] E.Y. Tsymbal, A. Gruverman, V. Garcia, M. Bibes, and A. Barthélémy, MRS Bull. **37**, 138 (2012).

[2] D.J. Kim, H. Lu, S. Ryu, C.W. Bark, C.B. Eom, E.Y. Tsymbal, and A. Gruverman, Nano Lett. **12**, 5697 (2012).

[3] J.M. López-Encarnación, J.D. Burton, E.Y. Tsymbal, and J.P. Velev, Nano Lett. **11**, 599 (2011).

[4] A. Gruverman, D. Wu, H. Lu, Y. Wang, H.W. Jang, C.M. Folkman, M.Y. Zhuravlev, D. Felker, M. Rzchowski, C.B. Eom, and E.Y. Tsymbal, Nano Lett. **9**, 3539 (2009).

[5] J. Li, N. Li, C. Ge, H. Huang, Y. Sun, P. Gao, M. He, C. Wang, G. Yang, and K. Jin, IScience **16**, 368 (2019).

[6] S. HORIUCHI and Y. TOKURA, Electr. Act. Mater. Med. Devices 81 (2016).

[7] K. Noda, K. Ishida, A. Kubono, T. Horiuchi, H. Yamada, and K. Matsushige, J. Appl. Phys. **93**, 2866 (2003).

[8] J. B. Torrance, J. E. Vazquez, J. J. Mayerle, V. Y. Lee, Phys. Rec. Lett. **46**, 4 (1981).

[9] S. Horiuchi, Y. Okimoto, R. Kumai, and Y. Tokura, J. Phys. Soc. Japan **69**, 1302 (2000).

[10] S. Horiuchi, R. Kumai, Y. Okimoto, and Y. Tokura, J. Am. Chem. Soc. **121**, 6757 (1999).

[11] S. Horiuchi, F. Ishii, R. Kumai, Y. Okimoto, H. Tachibana, N. Nagaosa, and Y.

Tokura, Nat. Mater. **4**, 163 (2005).

[12] R. Kumai, S. Horiuchi, Y. Okimoto, and Y. Tokura, J. Chem. Phys. **125**, (2006).

[13] S. Horiuchi, R. Kumai, and Y. Tokura, Angew. Chemie - Int. Ed. **46**, 3497 (2007).

[14] M.E. Lines and A.M. Glass, *Principles and Applications of Ferroelectrics and Related Materials* (Clarendon Press, Oxford, 1977).

[15] V.L. Ginzburg, Ferroelectr. Fundam. Collect. 131 (2007).

[16] Z.D. Zhou and D.Y. Wu, AIP Adv. **5**, (2015).

[17] R. Landauer, J. Appl. Phys. **28**, 227 (1957).

[18] R. Gysel, I. Stolichnov, A.K. Tagantsev, N. Setter, and P. Mokrý, J. Appl. Phys. **103**, (2008).

[19] P. Sharma, D. Wu, S. Poddar, T.J. Reece, S. Ducharme, and A. Gruverman, J. Appl. Phys. **110**, (2011).

[20] A.K. Tagantsev, I. Stolichnov, N. Setter, J.S. Cross, and M. Tsukada, Phys. Rev. B - Condens. Matter Mater. Phys. **66**, 1 (2002).

[21] S. V. Kalinin, A.N. Morozovska, L.Q. Chen, and B.J. Rodriguez, Reports Prog. Phys. **73**, (2010).

[22] T. Nagaya and Y. Ishibashi, J. Phys. Soc. Japan **60**, 4331 (1991).

[23] J. Schutrumpf, S. Zhukov, Y. A. Genenko, H. Von Seggern, J. Phys. D **45**, 165301 (2012).

[24] S. Horiuchi, F. Kagawa, K. Hatahara, K. Kobayashi, R. Kumai, Y. Murakami, and Y. Tokura, Nat. Commun. **3**, 1306 (2012).

[25] F. Bisti, A. Stroppa, S. Picozzi, and L. Ottaviano, J. Chem. Phys. **134**, (2011).

[26] S. Horiuchi, Y. Tokunaga, G. Giovannetti, S. Picozzi, H. Itoh, R. Shimano, R. Kumai, and Y. Tokura, Nature **463**, 789 (2010).

[27] X. Jiang, H. Lu, Y. Yin, X. Zhang, X. Wang, L. Yu, Z. Ahmadi, P.S. Costa, A.D. Dichiara, X. Cheng, A. Gruverman, A. Enders, and X. Xu, Appl. Phys. Lett. **109**, (2016).

[28] A. Bousseksou, G. Molnár, L. Salmon, and W. Nicolazzi, Chem. Soc. Rev. **40**, 3313 (2011).

[29] S. Bonhommeau, G. Molnár, A. Galet, A. Zwick, J.A. Real, J.J. McGarvey, and A. Bousseksou, Angew. Chemie - Int. Ed. **44**, 4069 (2005).

[30] S. Cobo, D. Ostrovskii, and S. Bonhommeau, J. Am. Chem. Soc. **130**, 9019 (2008).

[31] X. Zhang, A.T. N'Diaye, X. Jiang, X. Zhang, Y. Yin, X. Chen, X. Hong, X. Xu, and P.A. Dowben, Chem. Commun. **54**, (2018).

[32] C. Lefter, S. Rat, J.S. Costa, M.D. Manrique-Juárez, C.M. Quintero, L. Salmon, I. Séguy, T. Leichle, L. Nicu, P. Demont, A. Rotaru, G. Molnár, and A. Bousseksou, Adv. Mater. 7508 (2016).

[33] N. Moliner, L. Salmon, L. Capes, M.C. Muñoz, J.F. Létard, A. Bousseksou, J.P. Tuchagues, J.J. McGarvey, A.C. Dennis, M. Castro, R. Burriel, and J.A. Real, J. Phys. Chem. B **106**, 4276 (2002).

[34] X. Zhang, S. Mu, G. Chastanet, N. Daro, T. Palamarciuc, P. Rosa, J.F. Létard, J. Liu, G.E. Sterbinsky, D.A. Arena, C. Etrillard, B. Kundys, B. Doudin, and P.A. Dowben, J. Phys. Chem. C **119**, 16293 (2015).

[35] X. Jiang, G. Hao, X. Wang, A. Mosey, X. Zhang, L. Yu, A.J. Yost, A.D. DiChiara, A.T. N'Diaye, X. Cheng, J. Zhang, R. Cheng, X. Xu, and P.A. Dowben, J. Phys. Condens. Matter **31**, (2019).

[36] M. Hoffmann, F. P. G. Fengler, M. Herzig, T. Mittmann, B. Max, U. Schroeder, R. Negrea, P. Lucian, S. Slesazeck, T. Mikolajick, Nature, **565**, 464-467 (2019).

Chapter 2 Methods

2.1 Physical vapor deposition (PVD)

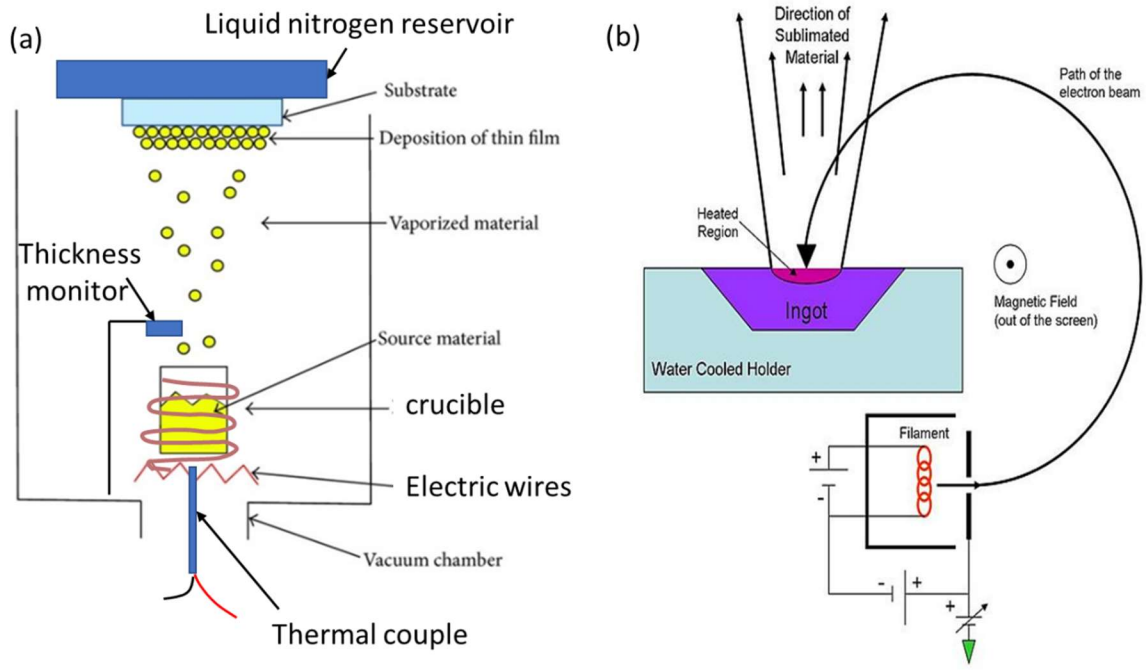

Fig. 2.1.1 (a) Sketch of PVD by resistive heating. (b) Sketch of PVD by electron beam heating[1].

A commonly applied method to grow organic thin film is spin coating, in which the material is diluted and dispensed on the spinning substrate. But in chemical methods, impurities in the film are inevitable and it is hard to realize out-of-plane multilayer growth[2]. We exploited physical vapor phase deposition (PVD) method, where the growth is processed in the ultrahigh vacuum (UHV) chamber, combined with RADAK resistive heating source and electron beam heating source.

Through the RADAK resistive heating source, the material (yellow part in Fig. 2.1.1 (a)) in the crucible evaporator is heated by flowing current in the surrounding electric wires (dark red curve line in Fig. 2.1.1 (a)). The source temperature is measured by the thermal couple right underneath the crucible. When the temperature reaches the

sublimation point, the material will evaporate and start to nucleate on the substrate in the UHV environment.

The evaporation rate is tracked by a thickness monitor, which is placed above the crucible. By measuring the oscillating frequency change of the thickness monitor pellet, the mass of the material deposited on the pellet can be obtained according to the relation $f = 2\pi\sqrt{\frac{k}{m}}$, where k is the spring constant of the pellet, and m is the total mass including the pellet and deposited material on the pellet. A tooling factor γ is introduced to derive the growth rate from the deposited mass. This factor depends on the solid angle of the substrate with respect to the heating source; it can be estimated by light reflection measurement or atomic force microscope. By considering the material density ρ, surface area of pellet s, and the time t cost for the deposition, the growth rate can be calculated as $r = \frac{d}{dt}(\frac{\gamma m}{\rho s})$. The growth rate is important for the morphology and crystallization of the thin film[3,4]. By controlling the growth time, we can obtain thin films with different thickness.

For the electron beam (ebeam) heating source[1] (Fig. 2.1.1 (b)), the electrons are ejected from the filament which holds high density current by a strong electric field, perpendicularly to the current direction. Through a strong magnetic field, these electrons with high energy are deflected to the crucible, where the metal pellets or insulator crystals are placed. When these hot electrons bombard the material in the crucible, the surface of the material is heated up. By controlling the emission current of the electron beam, the growth temperature and growth rate can be tuned.

With two RADAK resistive sources and 6 pockets of e-beam deposition, we can co-deposit different materials at the same time and fabricate multilayer electronic device

in-situ. By inserting different shadow masks during multilayer growth, the complex device structure can be achieved.

The substrate temperature is controlled by a proportional-integral-differential (PID) system with liquid nitrogen as the cooling power and a 50 Ω resistive heater as the heating power. By pumping the liquid nitrogen into the reservoir inside the chamber at different speed, and applying different currents in the resistor, the stabilized substrate temperature can vary from -190 °C to 100 °C. The substrate temperature is critical in the organic thin film growth, since it affects the absorption coefficient, material diffusion rate on surface and crystallization rate[5–8].

The sample holder can be rotated during the growth to achieve the homogeneous thin films. Multilayer devices can be fabricated with good thickness control.

2.2 Atomic Force Microscope (AFM) and Piezoresponse Force Microscope (PFM)

2.2.1 Experimental setup of AFM

Atomic force microscope (AFM) was first invented by Binning, Quate and Gerber in 1986[9,10]. It is used to detect the surface morphology in nanoscale by sensing the tip-sample interaction force. By maintaining a constant tip-surface interaction force, or the distance, through a feedback system via tuning the vertical position of the tip (traced by laser) during the scan, the topography of the sample surface can be detected. The experimental setup of AFM is shown in Fig. 2.2.1.

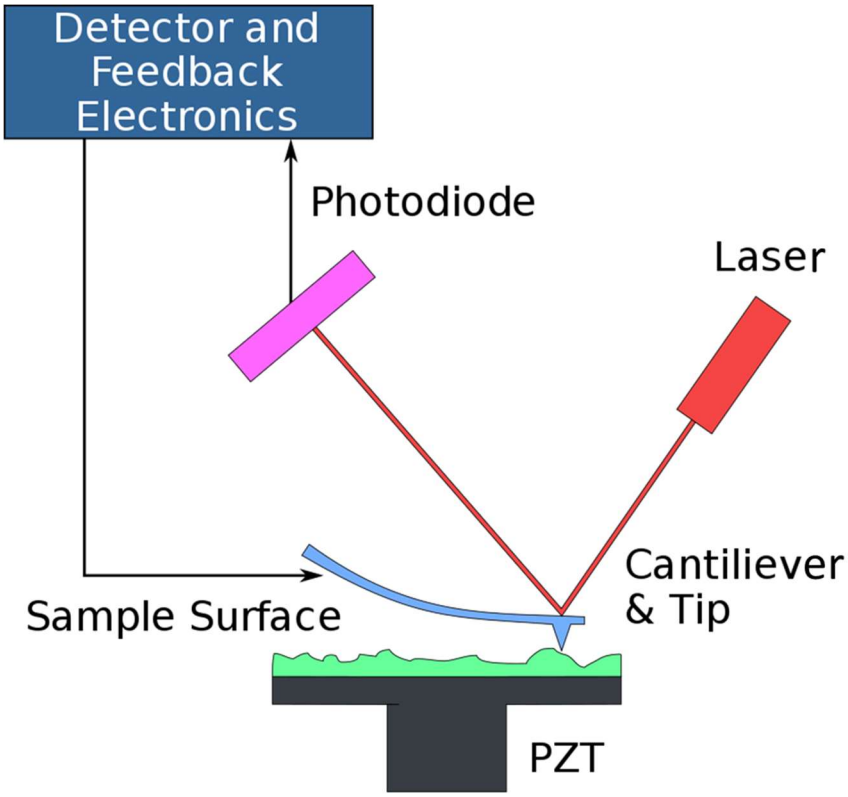

Fig. 2.2.1 The sketch of AFM setup[11].

2.2.2 Mechanism for AFM

Interaction between the tip and the sample surface is either repulsive or attractive, depending on the relative distance. These two types of atomic forces divide the AFM operational modes into three (Fig. 2.2.2): contact, non-contact and tapping modes.

The contact mode works in the repulsive force regime. It is a static mode, where the tip-surface separation is kept the same during the scanning across the surface of sample. Any change in sample surface will directly affect the tip position, and eventually the whole sample morphology is detected.

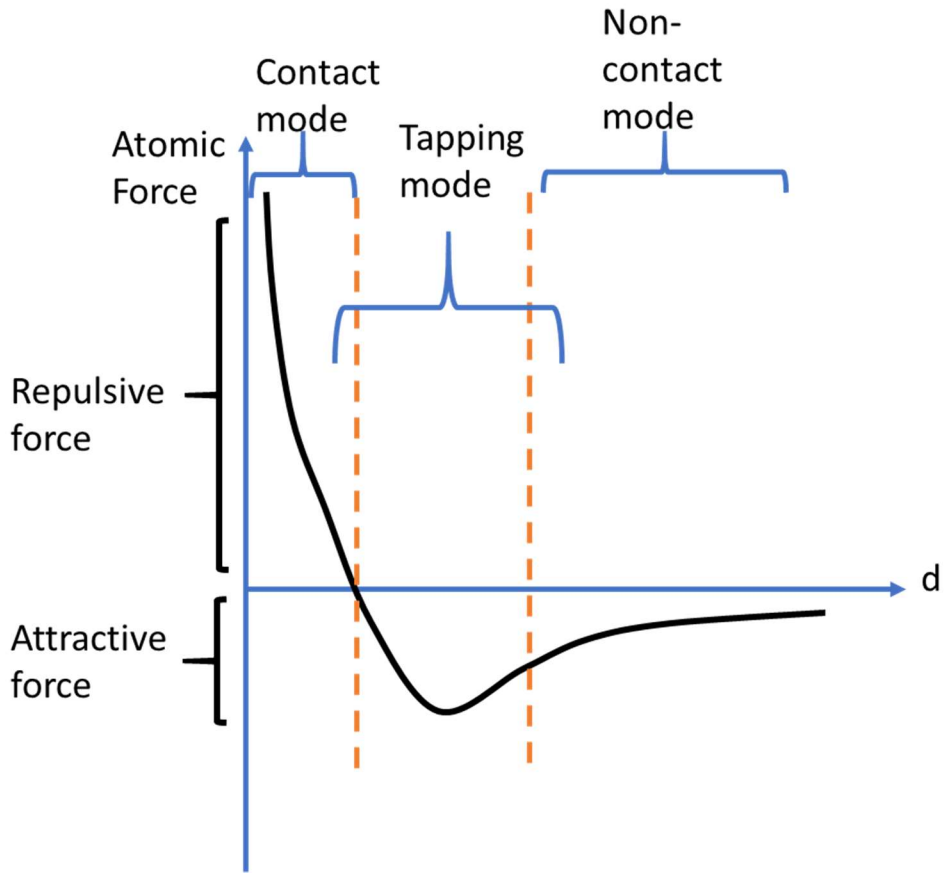

Fig. 2.2.2 Operation regions of different scanning modes.

Non-contact mode works in attractive force regime. It is a dynamic mode. The tip is kept at a small distance above the surface and an AC field is applied to it at the resonance frequency to detect the vertical tip position change due to surface morphology. When the tip feels the force from the sample surface, the amplitude, phase and resonance frequency of the AC voltage will be changed. To be specific, the resonance frequency of the cantilever can be expressed as[12]:

$$w^2 = w_0^2(1 - \frac{1}{k}\frac{\partial F_{ts}}{\partial d}). \qquad \text{Eq.2.2.1}$$

Here w_0 is the resonance frequency in free air, k is spring constant of cantilever, F_{ts} is the interaction force between tip and surface, and d is the separation between tip and surface. The small frequency change due to tip-surface interaction can be estimated as

$$\Delta w = w - w_0 = -\frac{w_0}{2k}\frac{\partial F_{ts}}{\partial d}. \quad \text{Eq.2.2.2}$$

To maintain the constant tip-surface distance, one can fix the oscillation amplitude and detect the resonance frequency change, or fix the resonance frequency slightly to the right due to attractive force, and detect the amplitude change. The amplitude change due to tip-surface interaction can be expressed as[12]:

$$\Delta A = \frac{2QA_0}{3\sqrt{3}(k-\frac{\partial F_{ts}}{\partial d})}\frac{\partial F_{ts}}{\partial d}, \quad \text{Eq.2.2.3}$$

where Q is the quality factor, and A_0 is the oscillation amplitude in free air.

The tapping mode is in the intermediate regime[13]. It is similar to non-contact mode but with much larger oscillation amplitude and left-shifted resonance frequency. When the tip is engaging the sample surface, the oscillation amplitude is significantly reduced due to tip-surface interaction. By the feedback loop, the oscillation amplitude can be a constant while the tip-surface distance changes accordingly. Tapping mode has higher sensitivity than non-contact mode and no scratching problem like in contact mode, so it is widely used.

2.2.3 Mechanism for PFM

Differing from the AFM, piezoresponse force microscope (PFM) uses a conductive material coated tip to detect the lattice distortion under the electric field. In piezoelectric materials, the strain **s** is coupled to the electric field **E** by the piezoelectric coefficient d, $s_j = d_{ij}E_i$. In ferroelectric materials, $d_{ij} = 2\varepsilon_{im}Q_{jmk}P_k$, where ε_{im} is the dielectric constant, Q_{jmk} is electrostriction coefficient, and P_k is the spontaneous polarization[14]. Depending on the structure symmetry of materials, some components of the piezoelectric coefficients can be zero or identical. For example, in tetragonal symmetry (point group: 4mm), the non-zero piezoelectric coefficients are d_{33}, d_{31}, d_{15}. The lattice deformation is

$\Delta L = s_3 L = \pm d_{33} V$, where $\pm$ represents the opposite directions of the polarization. Since the piezoelectric coefficient is typically very small, a lock-in amplifier is used.

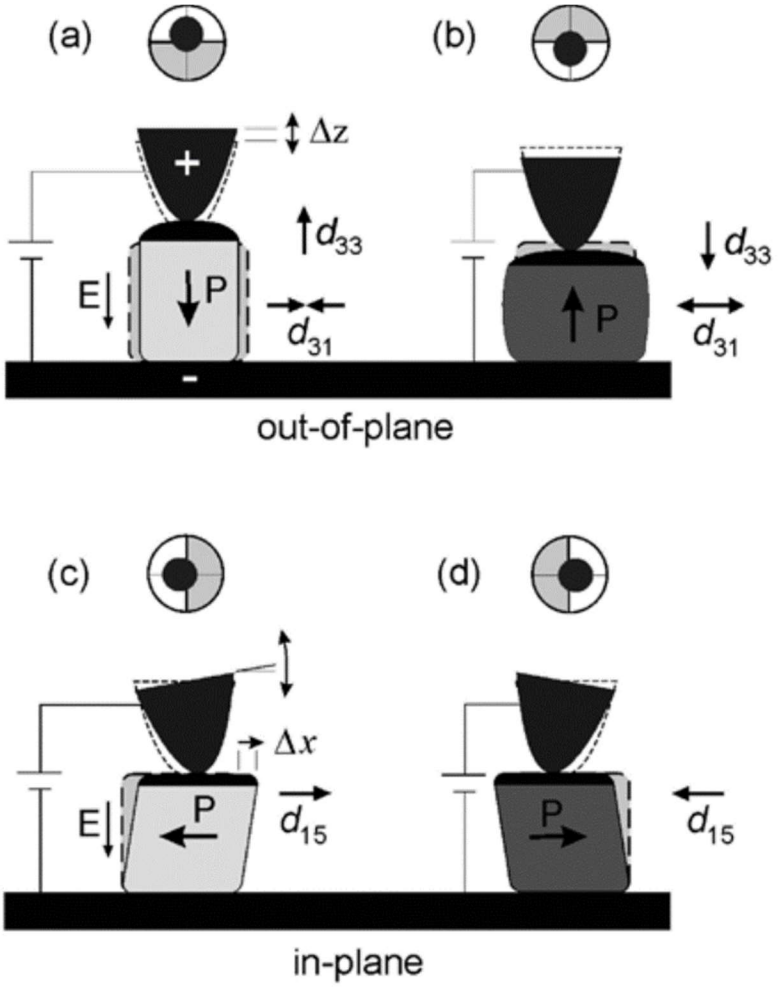

Fig. 2.2.3 Schematic diagram of vertical PFM (a) and (b) and lateral PFM (c) and (d)[19].

By applying an AC modulation voltage to the sample, the lattices will vibrate at the modulation frequency; this vibration can be filtered out by the lock-in amplifier system. Consider a simple case, where the applied AC voltage is $V_{ac} = V_0 \cos(wt)$. The vibration of lattice will be $d = A_{1w} \cos(wt + \phi)$, where A_{1w} is the first harmonic deflection vibration amplitude, and ϕ is the phase shift due to polarization direction.

Since the piezoelectric coefficient is a 3×3 tensor, under the vertical electric field, there will be both vertical and lateral vibrations (Fig. 2.2.3). The vertical displacement can be expressed as $Z = d_{33}V_0\cos(wt + \phi)$ and the lateral one is $X = d_{15}V_0\cos(wt + \phi)$.

For the thin films, the PFM signals are contributed from many factors besides the piezoelectric effect A_{pe}[15]. It's usually mixed with capacitive and coulombic interaction A_{cap} and non-local cantilever capacitive coupling A_{nl},

$$A = A_{pe} + A_{cap} + A_{nl}. \qquad \text{Eq.2.2.4}$$

The detection of domain wall is crucial to distinguish these three effects, since A_{pe} is only zero in the domain wall region. The domain wall is usually shown as the black contour lines in the PFM amplitude images. Lateral PFM amplitude and phase images of Croconic Acid on $NiCo_2O_4$ (NCO) is shown in Fig. 2.2.4.

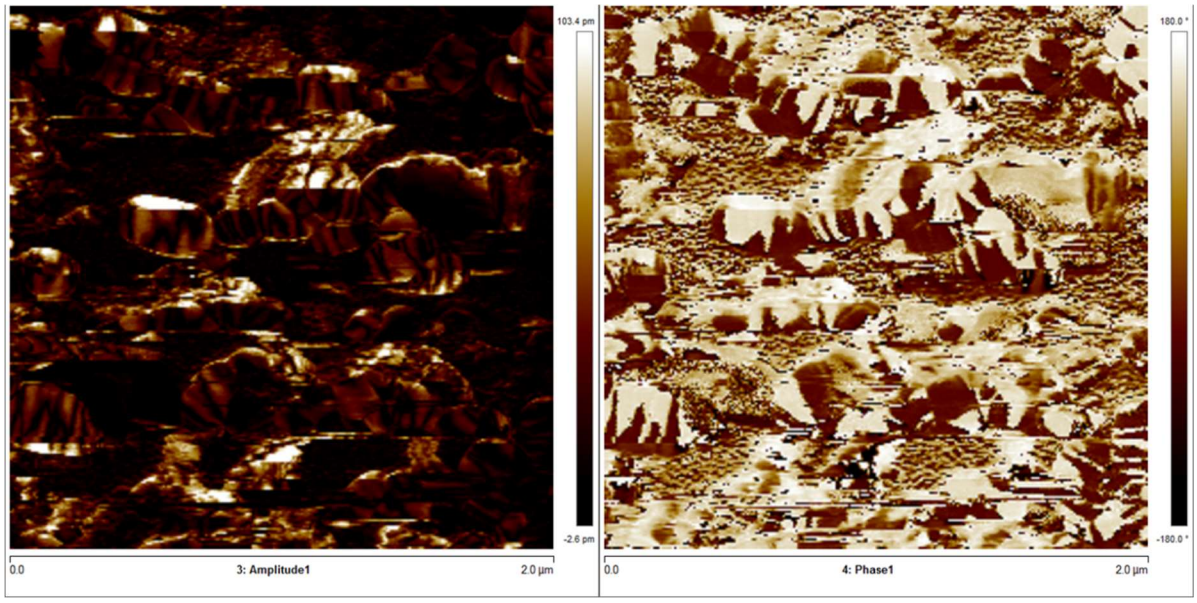

Fig. 2.2.4 Lateral PFM images of 40nm CA/NCO. Left panel shows the PFM amplitude of the film, and the right one shows the PFM phase of the film.

2.3 Time-resolved X-ray diffraction (XRD)

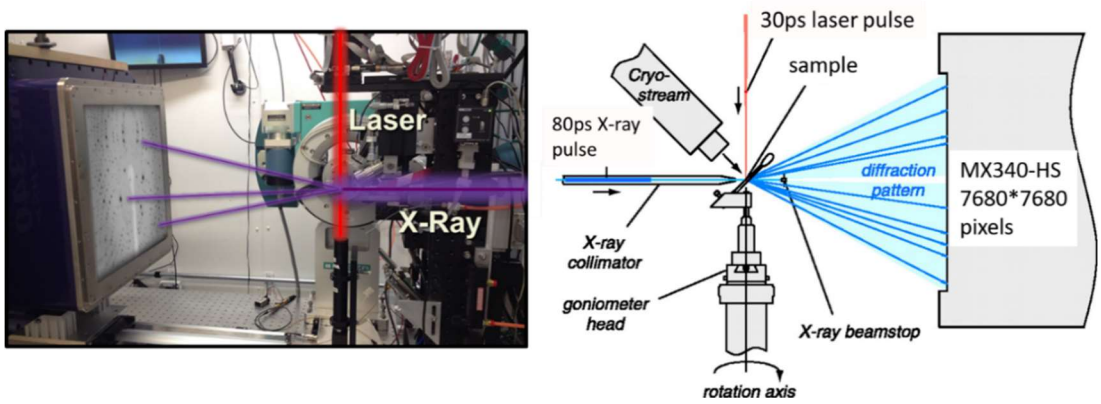

Fig. 2.3.1 (a) Experimental setup. (b) Sketch of time-resolved XRD experiment. Adopted from Ref. [20].

The time-resolved X-ray diffraction (XRD) system (Fig. 2.3.1 (a) taken in Argonne National Lab beamline 14-ID B[20]) is used to study the structural dynamics under the laser exposure. There are two origins of laser induced lattice distortion, the laser heating and photoexcitation. The first origin causes thermal expansion in the sample. By monitoring the relaxation time of thermal expansion, the existence of certain phonon modes can be unveiled, revealing the structural symmetry[16].

The other origin related to electronic structure causes the photostriction effect in ferroelectric materials. In ferroelectric materials, the unscreened bound charges produce a depolarization field in ferroelectric domains (Fig. 2.3.2 (a)). Photoexcitation induced electron-hole pairs are separated and move oppositely to the domain boundary under the effect of the depolarization field. This electron-hole separation process can cause an extra electric field in the material, which induces lattice expansion or contraction along the polarization direction depending on different piezoelectric coefficients $s_i = \frac{1}{d_{ij}} E_j$ (see Fig. 2.3.2 (b))[17].

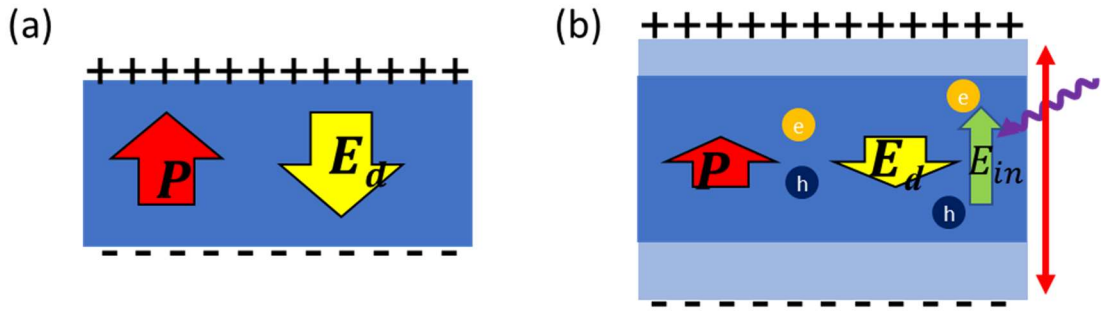

Fig. 2.3.2 Schematic diagram of (a) depolarization field and (b) photostriction effect in ferroelectric materials.

The setup (Fig. 2.3.1 (b)) is composed of four parts: laser, X-ray, sample holder and detector. The laser is placed right above the sample stage, whose wavelength, fluence and spot size can be tuned as required. The spot size is set to be larger than the X-ray footprint to ensure that all the materials detected are under laser exposure. The synchrotron X-ray has the wavelength of 1.0333Å and intensity of 12 keV. The X-ray beam is placed horizontally, perpendicular to the laser beam, and its beam size can be tuned all the way down to $20\ \mu m \times 20\ \mu m$. The position of the X-ray beam is detected by a phosphor diode.

The footprint of the laser and X-ray should cross at the sample surface. The laser pulse duration is 30 ps while the X-ray pulse duration is 80 ps. The time delay of X-ray with respect to the laser pulse can be set as short as 100 ps. By detecting the structure change for different delay time, the time resolved lattice information after photoexcitation is obtained. This pump-probe measurement is repeated for thousands of times to enhance the diffraction signal.

The sample position can be changed by a piezostage and the incident angle of X-ray can be tuned by a goniometer. Since the penetration depth of laser is much smaller than

that of X-ray, the incident angle of X-ray is set to be very small. However, the small incident angle will make the footprint of X-ray very long, sometimes longer than the sample size or the spot size of laser, so it is necessary to calculate the best incident angle before rotating the sample.

The beamline 14-ID B uses Ryonix MX340-HS for the detection of diffracted X-rays. This is a 2D screen with $34\ cm \times 34\ cm$ square size with$44\ \mu m \times 44\ \mu m$ pixel size. And the readout speed is 2.5 frames/second. This large 2D screen with high pixel resolution offers us more structural information and more precise structural dynamics in the pump-probe experiments.

The typical powder diffraction pattern from 2D detector is shown in Fig. 2.3.3.

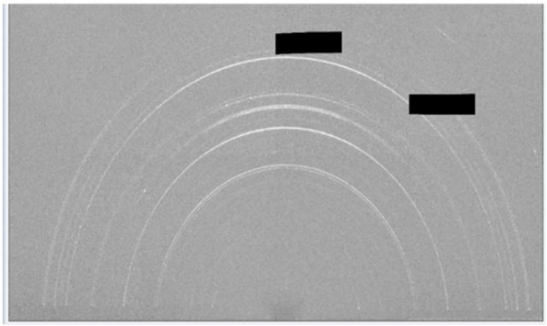

Fig. 2.3.3 2D powder diffraction pattern.

Evolution of the lattice parameters can by analyzed through diffraction data refinement. The first step is to convert the diffraction pattern to 2θ diffraction spectrum by calculating $2\theta = arctan\frac{r}{d}$, where r is the distance between the diffraction spot and the beam center, and d is the distance from detected spot on sample to the detector. By analyzing 2θ spectrum using Fullprof or GSAS software, the structure parameters, such as lattice constants, domain size, and even the relative atom positions can be revealed[18]. By

plotting the lattice information for different delay time in one figure, the time-resolved structural change due to photoexcitation can be obtained.

2.4 Reference

[1] K.S.S. Harsha, *Principles of Physics Vapor Deposition of Thin Films* (Elsevier, Great Britain, 2006, 2006).

[2] M. Biswas and S. Pei-Chen, in *Mod. Technol. Creat. Thin-Film Syst. Coatings* (2017).

[3] H. Guo, D. Sun, W. Wang, Z. Gai, I. Kravchenko, J. Shao, L. Jiang, T.Z. Ward, P.C. Snijders, L. Yin, J. Shen, and X. Xu, J. Appl. Phys. **113**, 0 (2013).

[4] A. Manuscript, (2019).

[5] G. Rojas, X. Chen, D. Kunkel, M. Bode, and A. Enders, Langmuir **27**, 14267 (2011).

[6] S.M. O'Malley, S.Y. Yi, R. Jimenez, J. Corgan, J. Borchert, J. Kuchmek, M.R. Papantonakis, R.A. McGill, and D.M. Bubb, Appl. Phys. A Mater. Sci. Process. **105**, 635 (2011).

[7] B. Krause, A.C. Dürr, F. Schreiber, H. Dosch, and O.H. Seeck, J. Chem. Phys. **119**, 3429 (2003).

[8] X. Jiang, H. Lu, Y. Yin, X. Zhang, X. Wang, L. Yu, Z. Ahmadi, P.S. Costa, A.D. Dichiara, X. Cheng, A. Gruverman, A. Enders, and X. Xu, Appl. Phys. Lett. **109**, (2016).

[9] G. Binnig, H. Rohrer, C. Gerber, and E. Weibel, Appl. Phys. Lett. **40**, 178 (1982).

[10] I. Goldie and H. Wetterqvist, Acta Orthop. Belg. **40**, 285 (1974).

[11] G. Binnig, US Pat. 4724318 (1986).

[12] H. Lu, *Polarization-Coupled Transport Behavior in Ultrathin Ferroelectric Heterostrutures* (2013).

[13] R. Hiesgen and K.A. Friedrich, PEM Fuel Cell Diagnostic Tools **3781**, 395 (2011).

[14] S. Hong, *Nanoscale Phenomenon in Ferroelectric Thin Films* (Springer, Germany, 2004).

[15] S. V. Kalinin and D.A. Bonnell, Phys. Rev. B - Condens. Matter Mater. Phys. **65**, 1 (2002).

[16] K. Sinha, Y. Zhang, X. Jiang, H. Wang, X. Wang, X. Zhang, P.J. Ryan, J.W. Kim, J. Bowlan, D.A. Yarotski, Y. Li, A.D. Dichiara, X. Cheng, X. Wu, and X. Xu, Phys. Rev. B **95**, 19 (2017).

[17] B. Kundys, Appl. Phys. Rev. **2**, (2015).

[18] B.D. Cullity and S.R. Stock, *Elements of X-Ray Diffraction* (Pearson, 1956).

[19] P. Khaenamkaew, I. K. Bdikin, A. L. Kholkin, S. Muensit, J. Sci. Technol. **30**, 59-63 (2008)

[20] https://www.aps.anl.gov/Time-Resolved-Research.

Chapter 3 Room Temperature Ferroelectricity in Continuous Croconic Acid Thin Films

3.1 Introduction

As mentioned in chapter 1, the Croconic Acid has many advantages: large spontaneous polarization, small coercive field and easy to sublimate. To explore the ferroelectric properties in CA thin films, in this chapter, we focus on the growth and characterizations of a fully covered, smooth and well-crystalized CA thin film on substrates.

This chapter is reproduced from [Appl. Phys. Lett. **109**, 102902 (2016); doi: 10.1063/1.4962278], with the permission of AIP Publishing.

Recent reports of room temperature ferroelectricity in croconic acid,[1] related oxocarbons,[2] benzimidazoles[3], and related hydrogen-bonded proton transfer systems[2] are currently accelerating the emergence of molecular ferroelectrics (MFE) as viable materials alternatives to inorganic ferroelectrics, such as the prototypical barium titanate, $BaTiO_3$. Importantly, croconic acid (CA), $C_5O_5H_2$, exhibits room temperature polarization of the order of 10 - 20 $\mu C/cm^2$ in bulk crystals, which is comparable to that of $BaTiO_3$, while at the same time the polarization switching fields are of practical order of magnitude.[3] The ferroelectric behavior of proton transfer organics like CA emerges from the resonance-assisted hydrogen bonding, specifically from the strong coupling between the protons in the hydrogen bonds and the π-electron system of the molecules that give them their dipole moments.[4]

MFEs have distinctive advantages over complex oxides and may replace oxides in some applications, with benefits in terms of flexibility, scalability, and sustainability.[5–7] The potential of MFEs to become viable material alternatives to inorganic ferroelectrics hinges on the availability of strategies to fabricate thin films with defined structure and morphology on a large scale, which at the same time preserve their ferroelectric properties. Vapor deposition, especially chemical vapor deposition polymerization, has been a method of choice for the fabrication of thin films of numerous organic polymers, including the popular ferroelectric polyvinylidene fluoride, PVDF.[8,9] However, previous work has ruled out, the possibility to utilize thermal evaporation growth techniques for CA because the decomposition temperature is lower than the melting point (≈177 °C). Another challenge is that the film growth tends to be three-dimensional, due to the weak interaction between the MFEs and most non-reactive inorganic substrates. Matrix-assisted pulsed laser deposition was performed as an alternative strategy for croconic acid thin films (100-200 nm thick), but without reporting the switchable ferroelectric behavior.[10]

Against these preconceptions and inspired by recent work on 2D layers of proton transfer ferroelectrics[11–13], we studied the growth of nanometer thin CA films using physical vapor deposition under high vacuum, over a large range of growth temperatures and film thicknesses. We show here that nanometer-thin quasi two-dimensional films of CA can be obtained by controlling the surface diffusion and nucleation during the growth. Importantly, room temperature ferroelectricity of these films is demonstrated in capacitor device structures as well as through local polarization manipulation on the nanometer scale using piezoresponse force microscopy.

3.2 Method

Nanometer thin films of CA were fabricated by physical vapor deposition (PVD) in high vacuum with an EvoVac system from Angstrom Engineering using Al_2O_3 as substrate, and alternatively using Al_2O_3 that has been buffered with either 30 nm $NiCo_2O_4$ (NCO)[14,15] or with 30 nm Al. The conducting NCO and Al buffer layers are of importance for the ferroelectric testing of the CA films where they will serve as bottom electrodes. The substrate temperature was controlled by a cartridge heater and a flow of liquid nitrogen (-150 °C to 70 °C). After deposition, the samples were warmed up to room temperature slowly (~ 0.1°C/min). Polarization imaging and local switching spectroscopy was performed using a commercial atomic force microscopy system (MFP-3D, Asylum Research) at resonant-enhanced PFM mode. PFM hysteresis loops were obtained at fixed locations on the film surface as a function of DC switching pulses (12 ms) superimposed on AC modulation bias. The polarization-voltage loop of an Al/CA film/Al/Al_2O_3 heterostructure was measured by a Sawyer-Tower method with a 1 Hz Sine wave input. Synchrotron X-ray diffraction on the CA film was carried out at beam line 14-ID-B at the Advanced Photon Source at room temperature.

3.3 Continuous CA thin film

We exploit the advantage of low sublimation temperature in high vacuum (1×10^{-7} Torr) to avoid molecule decomposition during evaporation,[1,3,4] as confirmed by the synchrotron X-ray diffraction measurements. As shown in Fig. 1(a), the general agreement between the diffraction spectrum of a film grown at a low source (crucible) temperature T_{src} (~130 °C) and that of the powder sample, indicates that the CA film is polycrystalline with the bulk crystal structure, suggesting that there is minimal thermal decomposition of the CA molecules during the sublimation process. Therefore, in this study a source

temperature of T_{src} ~ 130 °C has been selected for all growth experiments, which corresponds to a deposition rate of 1.2 Å/min.

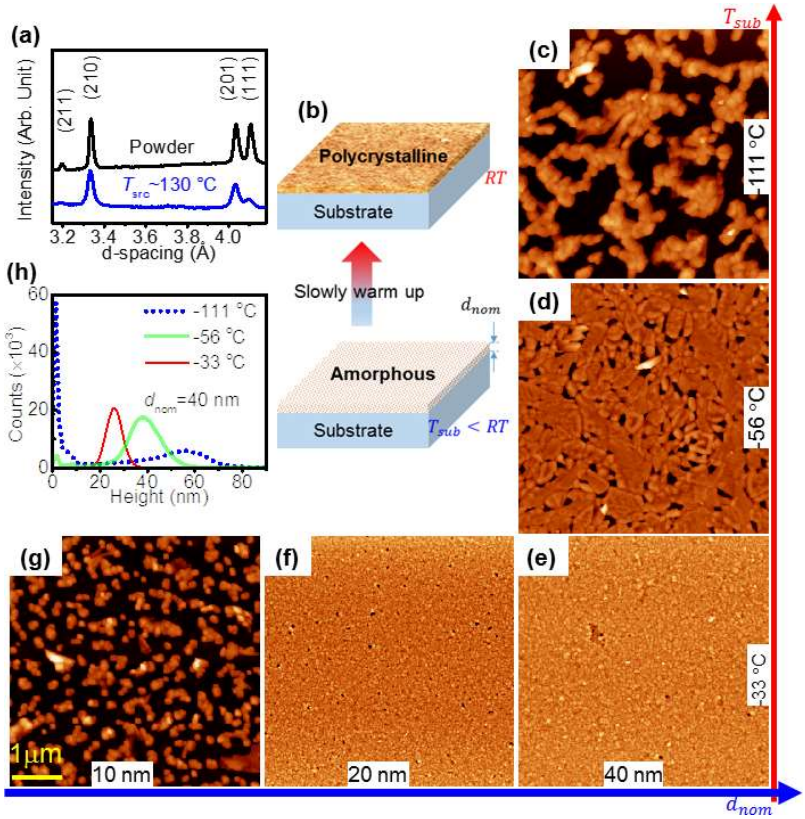

Fig. 3.3.1 Morphological and structural characterization of the croconic acid films. (a) X-ray diffraction of the CA films and that of the CA powder. (b) Schematics of the process of the film growth: deposition at low substrate temperature to obtain quasi 2D morphology followed by thermally induced crystallization after growth. The deposition rate was 1.2 Å/min. RT = room temperature. (c-e) The dependence of surface morphology on T_{sub} while keeping the nominal thickness d_{nom}=40 nm. (e-g) The dependence of the surface morphology on nominal film thickness (d_{nom}) at a growth temperature of T_{sub} =-33 °C. h) Distribution of the height analyzed from the images in (c-e).

The growth of continuous 2D films requires complete wettability of the substrate surface by the adsorbate layer.[16,17] This is often not the case for organics on non-reactive inorganic substrates so that nanometer film growth typically occurs in the Volmer Weber, or 3D growth mode.[18] A strategy to enforce complete surface coverage and thus 2D film growth is to limit the growth kinetics, which is determined by the ratio of the surface diffusivity and the deposition rate.[19] If the diffusivity is low enough (low substrate temperature), the growth is determined by kinetics, and metastable non-equilibrium structures can be achieved. Our strategy is thus to carry out a growth of a quasi-2D amorphous layer by deposition at low substrate temperature (T_{sub}) followed by a slow warming up of the substrate to room temperature (~0.1 °C/min) to crystallize the film to achieve grain sizes that are not much larger than the nominal film thickness (d_{nom}), as shown in Fig. 1(b). Both T_{sub} and d_{nom} are critical growth parameters, which were established experimentally in this study.

First, we investigated the effect of T_{sub} on the morphology of the films. The morphology of CA films (d_{nom} = 40 nm) grown on bare Al_2O_3 substrates at various temperatures T_{sub} is shown in Fig. 1(c)-1(e), where T_{sub} is low enough to significantly slow down the diffusion. The film morphology in Figs. 1(c) and 1(d) are characteristic for surface dewetting.[20–22] with much of the substrate surface still uncovered, despite the 40 nm nominal thickness. Therefore, as shown in Fig. 1(h), the height distributions of the morphologies of the films grown at T_{sub} = -56 °C and at T_{sub} =-111 °C show two peaks, where the first narrow peak corresponds to the substrate surface, and the second, broad Gaussian peak corresponds to the size-distribution of the CA crystallites, or grains. We attribute the low surface coverage at T_{sub} = -56 °C and at T_{sub} = -111 °C to low nucleation

rates. It appears that at higher temperature, T_{sub} = -33 °C (Fig. 1(e)), the nucleation rate is considerably higher, so that a large number of small crystallites becomes observable. Those crystallites coalesce so that in effect a quasi-2D morphology is achieved. At this coverage, the substrate surface is fully covered with only the CA grain peak being present in the histogram in Fig. 1(h). The RMS roughness of this film is 3.5 nm over a 5×5 μm^2 area. The average size of the grains, estimated from the AFM images, is approximately 60 nm (see Fig. S1 in the supplementary materials),[23] comparable to the nominal thickness of the film. For even higher substrate temperatures, T_{sub} > -33 °C, surface dewetting is observed again (see Fig. S2 in the supplementary materials),[23] which we attribute to the closer proximity to equilibrium growth due to the increased diffusion rate at higher temperature.

Next, we studied the dependence of the film morphology on the nominal film thickness d_{nom} in the kinetically limited growth regime. Fig. 3.3.1 (e)-1(g) show the AFM images of CA films of different d_{nom} grown with T_{sub} = -33 °C. While for d_{nom} = 10 nm there is still about 30% of the substrate surface uncovered, resulting in a discontinuous layer, the 20-nm-thick film appears to be nearly continuous, even though some defect pinholes are still present. The percentage of the uncovered surface area (bearing ratio) is 0.2% for the 20-nm-thick film, and <0.1% for d_{nom} > 20 nm.

Hence, to grow a continuous, or quasi-2D crystallized film using the strategy above, two conditions must be satisfied: (i) the substrate temperature must be in the range where the diffusion on the surface is suppressed during the deposition and a high nucleation rate can be achieved by annealing, and (ii) the nominal thickness of the film must be sufficiently large to achieve full surface coverage. For the present system of CA on Al_2O_3 (001) one sweet spot appears to be defined by ~20 nm of nominal thickness, deposited at T_{sub} = -33

°C. One implication is that a quasi-2D film can potentially always be achieved if T_{sub} is low enough to suppress the diffusion, as long as the film thickness is large enough to achieve full surface coverage. Therefore, this method may be applied to the growth of other molecular crystal thin films. This principle has long been established for the growth of metal thin films[19] and is demonstrated here for organic thin films as well. Identical growth parameters were used for the fabrication of CA films on different substrates, with very similar results regarding film and morphology.[23]

3.4 Ferroelectricity characterization

To test the ferroelectricity of the grown CA films, we measured the polarization hysteresis of the films using capacitor geometry first. We constructed first a capacitor device based on a 185 nm (thinner films were too leaky for the test) thin CA film grown on Al-buffered Al_2O_3, by depositing an Al top electrode over an area of ~ 0.5 mm^2. Fig. 3.4.1 (a) shows the polarization-voltage hysteresis of such an Al/CA/Al/Al_2O_3 heterostructure, which clearly demonstrates ferroelectricity of the vapor-phase grown CA films. The remnant polarization appears to be lower than that of single crystal, which is likely due to the polycrystalline nature of the CA film.

Local ferroelectricity of CA film was also studied using piezoresponse force microscopy (PFM) at room temperature.[24–26] PFM images representing the vertical (VPFM) and lateral (LPFM) amplitude and phase signals of a 35 nm thin film of CA are shown in Fig. 3.4.1 (c)-(f), along with a topographic image acquired from the same sample region (Fig. 3.4.1 (b)). The PFM data clearly show a polydomain structure, which appears to be closely related to the grain structure of the film. It may thus be concluded that each grain in the film is a single crystal of CA. Comparison of the VPFM (Fig. 3.4.1 (c) and (e))

and LPFM (Fig. 3.4.1 (d) and (f)) signals suggests that the orientation of the polar *c*-axis varies from grain to grain.

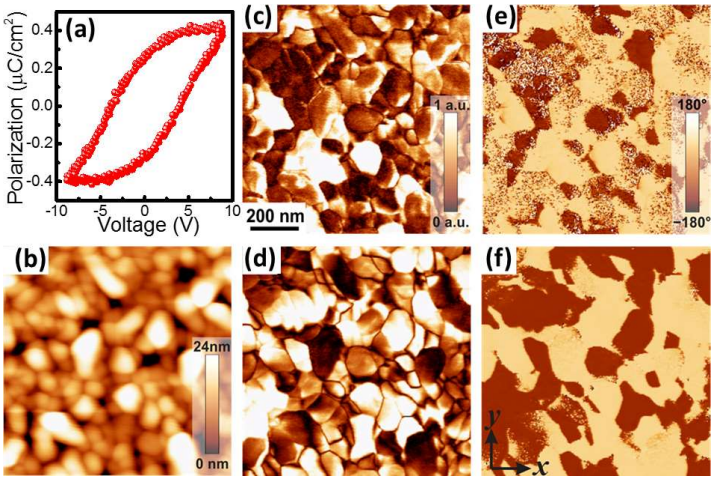

Fig. 3.4.1 (a) The polarization hysteresis of a 185 nm CA film in an Al/film/Al/Al_2O_3 capacitor geometry. (b) Surface topography of a 35-nm-thick croconic acid film on NCO/Al_2O_3. As-grown ferroelectric domain structures are shown in VPFM amplitude (c) and phase (e) images, and in LPFM amplitude (d) and phase (f) images in the same region as (b).

To study the effect of crystallite size on the ferroelectricity, we measured CA films grown at very lower T_{sub}, and found that the grains were sufficiently large to develop a polydomain state. An example of such a grain of a CA film grown at T_{sub} = -144 °C, which is over 300 nm in diameter, is shown in Fig. 3.4.2. A stripe domain pattern is apparent in the PFM amplitude and phase maps, indicating the presence of 180° domain walls separating areas of opposite polarization along the ferroelectric *c* axis.

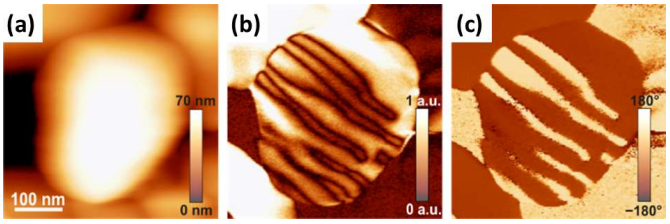

Fig. 3.4.2 Ferroelectric domain structure in a single grain. (a) Surface morphology, (b) LPFM amplitude and (c) LPFM phase.

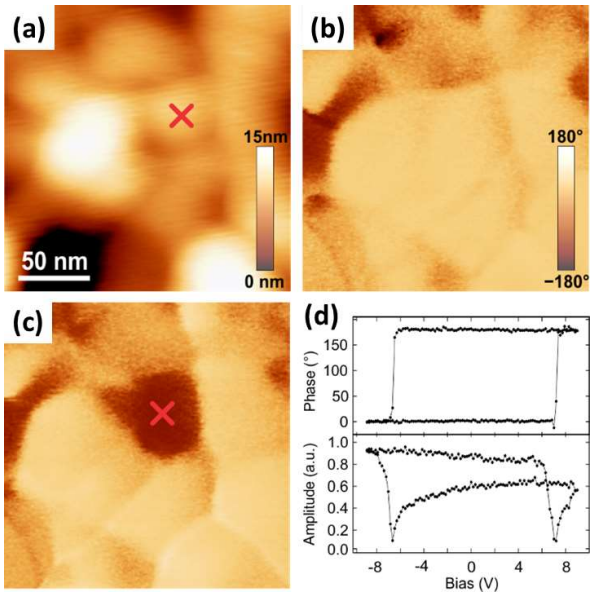

Fig. 3.4.3 Local switching of the ferroelectric polarization in a 35-nm-thick croconic acid film. (a) Surface morphology. (b) VPFM phase showing the as-grown domain structure. (c) Domain structure after application of a +9V pulse to a site marked by '×' in (a). (d) PFM switching spectroscopy showing piezoelectric hysteresis loops (upper panel – VPFM phase; lower panel – VPFM amplitude) with a coercive voltage of about 7V.

To further test the ferroelectric characteristics of the CA films we performed local polarization manipulation experiments. Voltage pulses were applied to selected grains in the film, with the PFM tip being in direct contact with the grain. Fig. 3.4.3 (a)-(c) shows the local manipulation of the polarization by application of an external +9V pulse to the tip

at position '×' in Fig. 3.4.3 (a), so that the ferroelectric polarization domain structure was reversed from that in Fig. 3.4.3 (b) to that in Fig. 3.4.3 (c). Further, Fig. 3.4.3 (d) shows the local PFM switching spectroscopy. The square phase-voltage hysteretic loop and butterfly-shaped amplitude-voltage curve demonstrate the ferroelectric switching occurred with a coercive voltage of ~7 V, signifying the switchable ferroelectric property of the CA thin films.

3.5 Conclusion

The obtained results demonstrate the growth of a continuous nanometer thin film of a proton transfer ferroelectric organics from the vapor phase. The key, by comparison to earlier studies that had ruled out this possibility, has been the careful sublimation of CA powder at temperatures that are far below the melting point. Conditions to achieve a quasi-2D film, or a quasi-continuous layer of crystallites, have been established: deposition at low substrate temperature to obtain 2D morphology and crystallization by slowly warming up to ambient temperature, which is expected to be applicable to other organic films as well. We have demonstrated that the as-grown films exhibit a spontaneous pattern of ferroelectric domains where it appears that the films grain structure corresponds with the domain structure. The significance of this study is in the establishment of a solvent-free growth protocol for room temperature organic ferroelectrics, the demonstration of their ferroelectric properties in real capacitor device, and the local manipulation of the polarization state with sub micrometer accuracy. We anticipate that our presented growth strategy can be adapted so that industrial fabrication at room-temperature is possible, by maintaining a kinetically limited film growth at significantly increased deposition rate. The

results are thus expected to accelerate the development of flexible and bendable ferroelectric thin films that may aide in the development of various applications.

3.6 References

[1] S. Horiuchi, Y. Tokunaga, G. Giovannetti, S. Picozzi, H. Itoh, R. Shimano, R. Kumai, and Y. Tokura, Nature **463**, 789 (2010).

[2] S. Horiuchi, R. Kumai, and Y. Tokura, Adv. Mater. **23**, 2098 (2011).

[3] S. Horiuchi, F. Kagawa, K. Hatahara, K. Kobayashi, R. Kumai, Y. Murakami, and Y. Tokura, Nat. Commun. **3**, 1308 (2012).

[4] J. Seliger, J. Plavec, P. Sket, V. Zagar, and R. Blinc, Phys. Status Solidi B Basic Solid State Phys. **248**, 2091 (2011).

[5] D.A. Bonnell, Science **339**, 401 (2013).

[6] W. Gao, L. Chang, H. Ma, L. You, J. Yin, J. Liu, Z. Liu, J. Wang, and G. Yuan, NPG Asia Mater. **7**, e189 (2015).

[7] Y. Noda, T. Yamada, K. Kobayashi, R. Kumai, S. Horiuchi, F. Kagawa, and T. Hasegawa, Adv. Mater. **27**, 6475 (2015).

[8] A. Kubono and N. Okui, Prog. Polym. Sci. **19**, 389 (1994).

[9] M.E. Alf, A. Asatekin, M.C. Barr, S.H. Baxamusa, H. Chelawat, G. Ozaydin-Ince, C.D. Petruczok, R. Sreenivasan, W.E. Tenhaeff, N.J. Trujillo, S. Vaddiraju, J. Xu, and K.K. Gleason, Adv. Mater. **22**, 1993 (2010).

[10] S.M. O'Malley, S.Y. Yi, R. Jimenez, J. Corgan, J. Borchert, J. Kuchmek, M.R. Papantonakis, R.A. McGill, and D.M. Bubb, Appl. Phys. A Mater. Sci. Process. **105**, 635 (2011).

[11] D.A. Kunkel, J. Hooper, B. Bradley, L. Schlueter, T. Rasmussen, P. Costa, S. Beniwal,

S. Ducharme, E. Zurek, and A. Enders, J. Phys. Chem. Lett. **7**, 435 (2016).

[12] D.A. Kunkel, J. Hooper, S. Simpson, G.A. Rojas, S. Ducharme, T. Usher, E. Zurek, and A. Enders, Phys. Rev. B **87**, 041402 (2013).

[13] S. Beniwal, S. Chen, D.A. Kunkel, J. Hooper, S. Simpson, E. Zurek, X.C. Zeng, and A. Enders, Chem. Commun. **50**, 8659 (2014).

[14] P. Silwal, L. Miao, I. Stern, X. Zhou, J. Hu, and D. Ho Kim, Appl. Phys. Lett. **100**, 032102 (2012).

[15] P. Silwal, L. Miao, J. Hu, L. Spinu, D. Ho Kim, and D. Talbayev, J. Appl. Phys. **114**, 103704 (2013).

[16] E. Bauer and J.H. van der Merwe, Phys. Rev. B **33**, 3657 (1986).

[17] M. Copel, M.C. Reuter, E. Kaxiras, and R.M. Tromp, Phys. Rev. Lett. **63**, 632 (1989).

[18] G. Rojas, X. Chen, D. Kunkel, M. Bode, and A. Enders, Langmuir **27**, 14267 (2011).

[19] J. V Barth, G. Costantini, and K. Kern, Nature **437**, 671 (2005).

[20] A.C. Durr, F. Schreiber, M. Kelsch, H.D. Carstanjen, and H. Dosch, Adv. Mater. **14**, 961 (2002).

[21] A.C. Durr, F. Schreiber, M. Kelsch, H.D. Carstanjen, H. Dosch, and O.H. Seeck, J. Appl. Phys. **93**, 5201 (2003).

[22] B. Krause, a. C. Dürr, F. Schreiber, H. Dosch, and O.H. Seeck, J. Chem. Phys. **119**, 3429 (2003).

[23]See Supplementary Material at Http://dx.doi.org/ for the Details.

[24] A. Gurverman, O. Auciello, and H. Tokumoto, Annu. Rev. Mater. Sci. **28**, 101 (1998).

[25] D.A. Bonnell, S. V Kalinin, A.L. Kholkin, and A. Gruverman, MRS Bull. **34**, 648 (2009).

[26] A. Gruverman and S. V. Kalinin, J. Mater. Sci. **41**, 107 (2006).

Chapter 4 Long-lived photostriction effect in an organic ferroelectric material

4.1 Introduction

In chapter 3, successful fabrication of the high quality ferroelectric Croconic Acid (CA) thin films has been achieved and discussed. In this chapter, we will investigate its electron-phonon interaction in a dynamic study. This will help us to gain microscopic understandings of its ferroelectric properties and corresponding strong relation to its crystal structure.

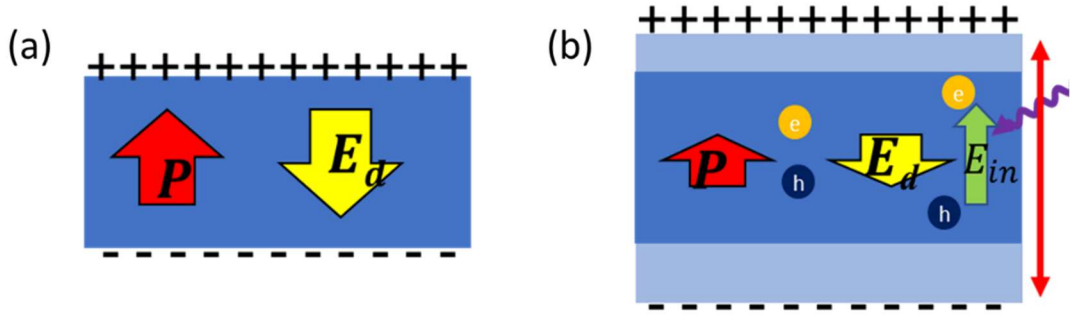

Fig. 4.1.1 Mechanism of photostriction effect in ferroelectric materials. (a) Poled ferroelectrics with polarization P and depolarization field E_d. (b) Photostriction effect due to photovoltaic and inverse piezoelectric effect.

Photoexcitation, distinguished from other external stimuli because of its local and fast switching, is a common way to detect the transient conductivity, magnetism and structure of the crystals by introducing change in the electronic structure[1,2,3,4]. To be specific, in ferroelectric materials, the structure is distorted due to the movement (along the polarization direction) of the electrons generated in the process of photoexcitation[5]. Under the depolarization field, photoexcited electrons can be separated and transfer to the ferroelectric domain boundary, resulting in the voltage drop across the ferroelectric domain.

This is the photovoltaic effect in ferroelectric material. Meanwhile, applied electric field can induce displacements of atoms in ferroelectric materials, producing strain and leading to the inverse piezoelectric effect. Combining these two effects, the photovoltage-associated electric field can induce strain on the lattice and alter the lattice structure. The lattice change in ferroelectric materials due to the superposition of photovoltaic and inverse piezoelectric effects is called photostriction (Fig. 4.1.1).

In principal, the electron movement can be detected via photovoltage in open circuit or photocurrent in short circuit[6,7]. However, the photoexcitation induced electron movement, and the associated structural change, have not been fully studied. In our work, we studied the photostriction effect in an organic ferroelectric material, Croconic Acid (CA), whose ferroelectricity comes from distorted π electron in molecules and intermolecular hydrogen bonds. Due to proton transfer in the hydrogen bonds, the polarization can be switched along the *c* axis[8]. Under the illumination with photon energy larger than the bandgap, the electrons in CA can be excited from the HOMO to LUMO level[9]. Those photoexcited electrons will move under the depolarization field to the domain boundaries and screen the bound charges, which provides an external field that elongates the lattice along c axis.

The photostriction effect of CA is studied by time-resolved x-ray diffraction (XRD) in Argonne National Lab, which monitored the lattice change under the laser illumination and recorded the relaxation time after the laser was turned off. From our results, the photostriction effect along *c* axis is the largest, which is different from thermal expansion. Surprisingly, the relaxation time after photoexcitation is very long, which is in the scale of minutes. This ultralong relaxation time has never been reported in other ferroelectric

materials. To resolve this ultralong relaxation time, we investigated the charge diffusion and recombination processes by measuring the shift of local hysteresis loop and the relaxation time of photocurrent.

4.2 Method

Nanometer thin films of CA were fabricated on different substrates by physical vapor deposition (PVD) in high vacuum ($1e^{-7}\ Torr$) with an EvoVac system from Angstrom Engineering[10]. We grew 300 nm CA on Al_2O_3 (room temperature, RT) for time resolved XRD, 140 nm on patterned Au/SiO_2 substrate (RT) for photocurrent measurements, and 40 nm on conductive $NiCo_2O_4$ (NCO) substrate (-30 °C) for PFM study. The substrate temperature was controlled by a cartridge heater and a flow of liquid nitrogen. The thickness of the samples is obtained by a thickness monitor. For the -30 °C sample deposition, after deposition, the samples were warmed up to RT slowly (~ 0.2 °C/min) and annealed at 30°C for 1h for better crystallization.

The time-resolved synchrotron XRD (as shown in Fig. 4.3.1 (a)) on the CA film was carried out at beam line 14-ID-B at the Advanced Photon Source of Argonne National Lab at room temperature. The sample was placed 32 cm from the detector. Optical excitation was provided by laser pulses with fluence 2 μj/mm^2 and a central wavelength of 330 nm. Incident x-ray pulses of 12 keV were focused to 75 um full-width half-maximum (FWHM) in diameter with incident angle 1.5 deg, overfilled by a 120 um x 3400 um FWHM pump laser spot. The delayed time of x-ray with respect to the laser was electronically controlled. The sample was exposed to laser for 1800 s with rep rate 500 Hz and the x-ray was used to test its structure every 100 seconds. After the laser was turned off, X-ray continued to shoot until the structure relaxed back. The diffraction rings on the

2D detector was converted into intensity vs d-spacing graph. The lattice constants at different time were refined in Fullprof program by fitting their peak position, intensity and width.

The photocurrent in DC circuit was measured by Keithley 236 and in AC by the impedance analyzer Solartron 1260. 60 nm Al_2O_3 protection layer was grown on top of CA. The dimension of conduction channel is $10\ \mu m \times 100\ nm \times 80\ nm$. The light source was a commercial diode laser with photon energy of 3.1 eV and intensity on the sample surface was 140 mW/cm^2. For the DC measurement, 1 V was applied across the photoconduction channel; and for the AC measurement, 1 V AC voltage with frequency of 100 Hz was applied.

Polarization imaging and local switching spectroscopy were performed using a commercial atomic force microscopy system (MFP-3D, Asylum Research) in the resonant-enhanced piezoresponse force microscope (PFM) mode. PFM hysteresis loops were obtained at fixed locations on the film surface by superimposing AC modulation on different DC bias (12 ms). The UV light used in the PFM study had the wavelength around 390 nm and intensity of 15 mW/cm^2.

4.3 Photostriction

After converting the diffraction pattern to lattice parameters, we can plot the time dependent lattice change during photoexcitation and relaxation processes, as shown in Fig. 4.3.1 (b) and (c). When the laser is turned on, the lattice expands along three axes. This lattice expansion is different from the thermal expansion in CA. Due to structure anisotropy, the lattice expansion along b axis should be the largest in thermal expansion. But in our result, the lattice expansion along three axes is similar. The absence of structure anisotropy

can be explained by the proton transfer induced lattice distortion. There are two kinds of hydrogen bonds in CA, one is at the herringbone along the c axis, and the other is in the molecular plane, which has the largest proportion along a axis. The proton transfer due to movement of photoexcited electrons change length and angle of the hydrogen bonds. This will induce lattice distortion, mostly along the *c* and *a* axis, compensating the structure anisotropy, resulting in similar expansion ratio along three directions. Also, we find that the lattice expansion saturates around 400 s, which indicates that the light induced lattice distortion reaches equilibrium. This is another evidence that this lattice expansion is mainly due to the photostriction effect, rather than laser heating. In a word, we demonstrated the lattice expansion by photostriction effect in ferroelectric proton-transfer material CA. The lattice change is on the order of 10^{-4}, and the saturation time is around 7 mins.

A more interesting part of the photostriction effect in CA is the relaxation. After the laser is turned off, the lattice doesn't relax back as shortly as in other ferroelectric materials[3,4,11]. In our case, the lattice expansion persists for 20 min before it starts relaxation. This ultralong persistent time has rarely been found in the similar materials[12,13,14,15].

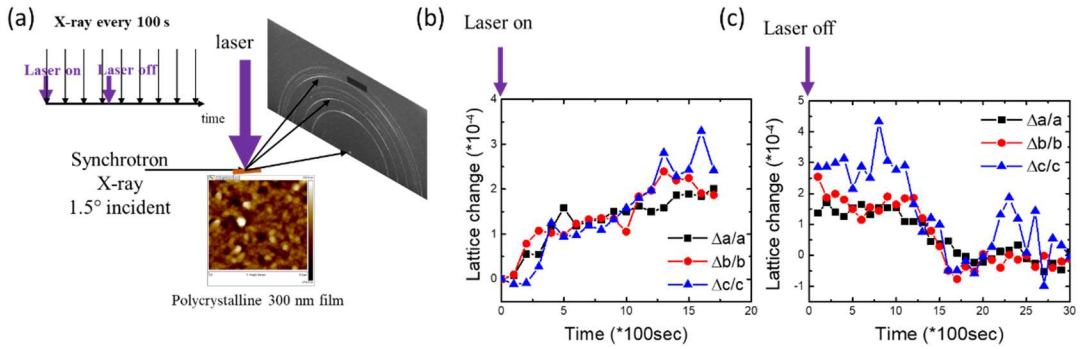

Fig. 4.3.1 Time-resolved XRD of CA. (a) Experimental setup. (b) Lattice expansion during photoexcitation. (c) Relaxation process.

4.4 Dynamics of charge carriers

To understand the long persistent time, we need to consider the four steps that the electrons would experience from photoexcitation to recombination. The first step is photoexcitation. Electron-hole pairs are created via photon absorption when the photon energy is slightly higher than the energy gap between HOMO and LUMO levels (Fig. 4.5.1 (a) (1)). Then the electrons and holes separate and drift oppositely due to the strong depolarization field, as shown in Fig. 4.5.1 (a) (2). The drift velocity is faster than the recombination rate, so the electron-hole pairs can be separated and become free charge carriers. Due to strong depolarization field, the charge separation can be very large even at the domain boundary. This charge separation will only stop when the drift electrons and holes completely screen the bound charges at the domain boundaries and cancel out the depolarization field. At this moment, the lattice expansion due to movement of photoexcited charges is saturated. After this, the laser is turned off, the photoexcited electrons and holes will diffuse back (Fig. 4.5.1 (a) (3)). The diffusion rate depends on the diffusion barrier, which can be induced by local electrostatic potential profile due to molecular structure change or lattice distortion. At last, the electron and hole meet and recombine through photoemission or thermal relaxation (Fig. 4.5.1 (a) (4)). The recombination rate depends on the probability of the dipole transition, which depends on the symmetry of spin and orbital wavefunctions of initial and final states.

4.5 Possible mechanisms of long persistence

4.5.1 Models of mechanisms

We then propose two possible mechanisms to explain the long persistent time. The first one is related to the triplet recombination process of the spin decoherent electrons (Fig.

4.5.1 (b)). Spin decoherence may happen during electron drift and diffusion process[15,16,17]. Even though the spin-orbit coupling in organic materials is typically small due to small atomic number, the probability of spin flip is increased when the electrons jump from the one molecular orbit to another for multiple times under depolarization field. Due to the occurrence of spin decoherence, when the electrons diffuse back, their spin direction is parallel with the spin polarization of the electrons in the HOMO level. This state is called the triplet state. According to the selection rule, the electron cannot directly jump back to the HOMO level. So, the recombination process of triplet state will take longer time because of the smaller transition probability.

The other mechanism is the formation of diffusion barrier due to the molecular structure change during charge transfer (Fig. 4.5.1 (c)). When an electron is excited to LUMO level by a photon, it can transfer to the right molecule under the depolarization field and attract the proton to deflect from its original position, since the proton in the hydrogen bonds can be treated as a positive center with a large charge density. This proton deflection will cause the change in the length and angle of the hydrogen bond, leading to the lattice distortion and enhancing a diffusion barrier. When the laser is turned off, the barrier would prevent the photoexcited electrons from diffusing back, lowering the diffusion rate and increasing the whole relaxation time. The proton deflection in hydrogen bonds during photoexcitation in CA single crystal has been inferred in a pump-probe experiment with second harmonic generation as the probe[18].

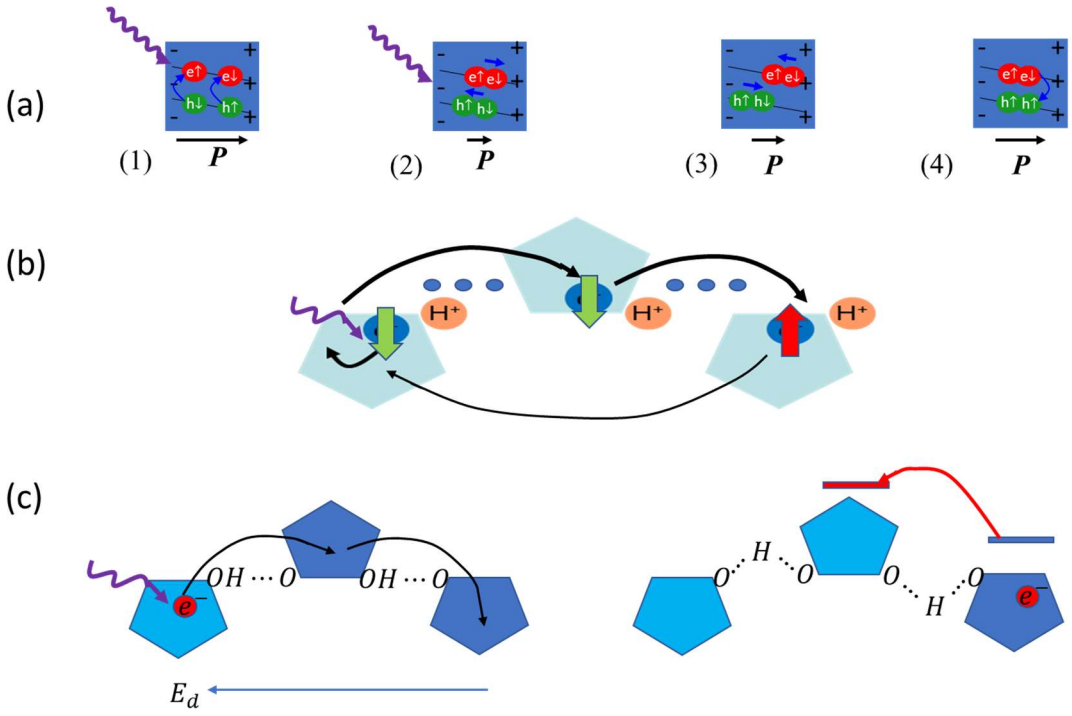

Fig. 4.5.1 Behavior of charge carriers. (a) (1) Photoexcitation, (2) Charge drift, (3) Charge diffusion, (4) Recombination. (b) Spin decoherence during charge transfer. (c) Diffusion barrier due to lattice distortion.

4.5.2 Photocurrent

We conducted the photocurrent measurement (Fig. 4.5.2 (a)) to detect the long recombination time, as discussed in the first mechanism. From the DC measurement in Fig. 4.5.2 (b), we can get the static photocurrent, which is around 10 $\mu A/cm^2$. However, in DC measurement, the RC constant of CA is very large, so the measured relaxation time is not totally contributed by the recombination time of photoexcited electrons. To solve this problem, we also measured the photoconductivity using the AC voltage (Fig. 4.5.2 (c)). We can clearly see that the recombination time τ is around 4 seconds, much longer than that of other organic optoelectronic materials[19]. This long recombination time is related to

the triplet recombination process, which indicates the existence of spin decoherence during charge transfer.

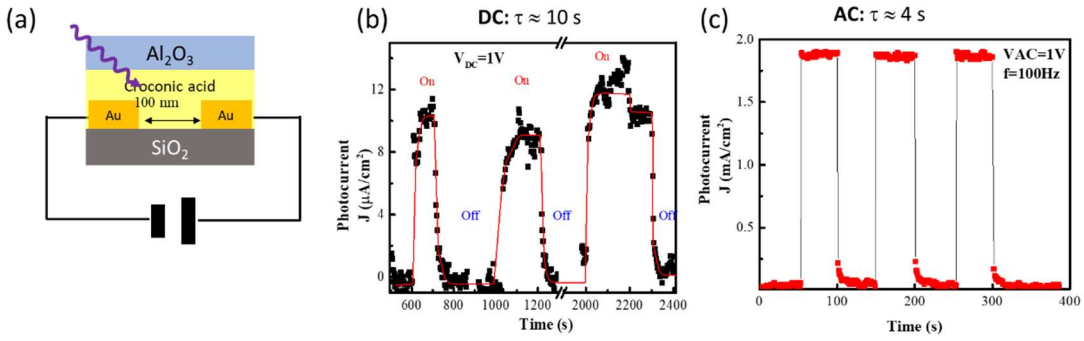

Fig. 4.5.2 Photocurrent measurement. (a) Device structure, (b) Photocurrent in DC circuit, (c) Photocurrent in AC circuit.

4.5.3 Charge accumulation

To verify the second mechanism, we used PFM to detect shift of local hysteresis loop under UV light (Fig. 4.5.3). The shift reflects the electron accumulation at the domain boundary. Before turning on the UV light, the polarization of CA domain is aligned to point up, leading to an initial downward depolarization field. When the UV light is turned on, the photoexcited electrons move according to the depolarization field and form photo-induced field which points up. The diffusion rate of these photoexcited electrons is slow. Thus, the charge carriers will stay at the domain boundaries in the fast sweeping (ms) biased electric field, and this will keep the induced field along the upward direction[20]. The total field, $\boldsymbol{E_{ex} + E_{de} + E_{ph}}$, should equal the coercive field $\boldsymbol{E_c}$ to switch the polarization, where $\boldsymbol{E_{ex}}$ is the external field needed to switch the polarizations, $\boldsymbol{E_{de}}$ is the depolarization field, and $\boldsymbol{E_{ph}}$ is the induced electric field by photoexcited charges accumulated at domain boundary. When the polarization is switched from up to down (Fig. 4.5.3 (a)), the magnitude of the needed external field is $E_{ex} = E_C - E_{de} + E_{ph}$; however, when the

polarization is switched from down to up (Fig. 4.5.3 (b)), the magnitude is $E_{ex} = E_C - E_{de} - E_{ph}$. It's clear that the magnitude of the needed switching field in the two cases becomes different. In the PFM study, the difference is reflected by the right shift of the hysteresis loop. With longer exposure time, more charge carriers will move to the domain boundaries, providing larger induced electric field. As a result, the hysteresis loop keeps shifting to the right (Fig. 4.5.3 (d)). The time constant for the charge diffusion process is around 20 min, as can be obtained from the relaxation process after light is off (Fig. 4.5.3 (f)). This time scale is similar to the persistent time in the photostriction measurement, which indicates the existence of diffusion barrier during charge transfer.

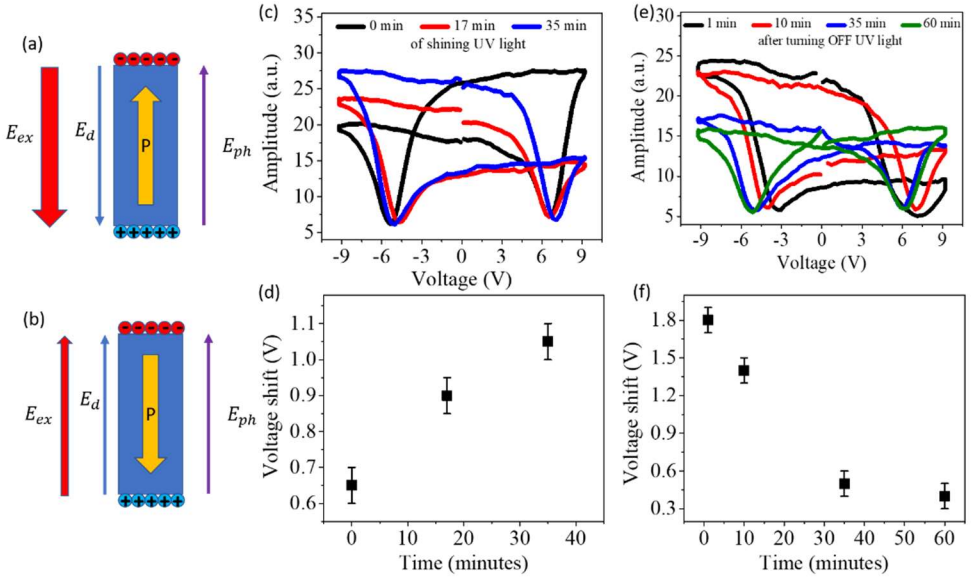

Fig. 4.5.3 Local switching hysteresis loop under luminescence. (a) Schematic diagram of switching polarization from up to down. (b) Schematic diagram of switching polarization from down to up. (c) Amplitude of vertical PFM (VPFM) hysteresis loop under UV light. (d) Exposure time dependence of switching voltage shift. (e) Amplitude of vertical PFM (VPFM) hysteresis loop after UV light. (f) Time dependence of voltage shift in relaxation process.

4.6 Conclusion

We demonstrated the photostriction effect, the superposition of photovoltaic and inverse piezoelectric effect, in an organic ferroelectric material CA. The most interesting is the ultralong persistent time. To explain this ultralong relaxation time, the mechanisms of spin decoherence during charge transfer and formation of diffusion barrier by lattice distortion are considered and investigated. This work reveals that proton-transfer ferroelectrics could be good candidates for the long persistent optoelectronic device.

4.7 References

[1] B. Kundys, M. Viret, D. Colson, and D.O. Kundys, Nat. Mater. **9**, 803 (2010).

[2] W.R. Diluzio, G.M. Whitesides, J.A. Hubbell, N.A. Peppas, J.H. George, D.J. Mooney, S. Sen, H.L. Sweeney, D.E. Discher, M.J. Bissell, J. Hubbell, K.S. Anseth, A.H. Zisch, M.P. Lutolf, J.L. Wrana, J.A. Hubbell, R. Langer, D.J. Mooney, J.S. Miller, J.L. West, M.S. Shoichet, M.S. Shoichet, I.M. Plitz, R.A. Frantz, P.A. Lovell, K.S. Anseth, and J. Elisseeff, **324**, 63 (2009).

[3] D. Daranciang, M.J. Highland, H. Wen, S.M. Young, N.C. Brandt, H.Y. Hwang, M. Vattilana, M. Nicoul, F. Quirin, J. Goodfellow, T. Qi, I. Grinberg, D.M. Fritz, M. Cammarata, D. Zhu, H.T. Lemke, D.A. Walko, E.M. Dufresne, Y. Li, J. Larsson, D.A. Reis, K. Sokolowski-Tinten, K.A. Nelson, A.M. Rappe, P.H. Fuoss, G.B. Stephenson, and A.M. Lindenberg, Phys. Rev. Lett. **108**, 1 (2012).

[4] H. Wen, P. Chen, M.P. Cosgriff, D.A. Walko, J.H. Lee, C. Adamo, R.D. Schaller, J.F. Ihlefeld, E.M. Dufresne, D.G. Schlom, P.G. Evans, J.W. Freeland, and Y. Li, Phys. Rev. Lett. **110**, 1 (2013).

[5] B. Kundys, Appl. Phys. Rev. **2**, (2015).

[6] Y. Yuan, Z. Xiao, B. Yang, and J. Huang, J. Mater. Chem. A **2**, 6027 (2014).

[7] C. Rankin, C.H. Chou, D. Conklin, and D.A. Bonnell, ACS Nano **1**, 234 (2007).

[8] S. Horiuchi, Y. Tokunaga, G. Giovannetti, S. Picozzi, H. Itoh, R. Shimano, R. Kumai, and Y. Tokura, Nature **463**, 789 (2010).

[9] F. Bisti, A. Stroppa, F. Perrozzi, M. Donarelli, S. Picozzi, M. Coreno, M. De Simone, K.C. Prince, and L. Ottaviano, J. Chem. Phys. **138**, 1 (2013).

[10] X. Jiang, H. Lu, Y. Yin, X. Zhang, X. Wang, L. Yu, Z. Ahmadi, P.S. Costa, A.D.

Dichiara, X. Cheng, A. Gruverman, A. Enders, and X. Xu, Appl. Phys. Lett. **109**, (2016).

[11] Y. Zhou, L. You, S. Wang, Z. Ku, H. Fan, D. Schmidt, A. Rusydi, L. Chang, L. Wang, P. Ren, L. Chen, G. Yuan, L. Chen, and J. Wang, Nat. Commun. **7**, 1 (2016).

[12] Q. Burlingame, C. Coburn, X. Che, A. Panda, Y. Qu, and S.R. Forrest, Nature **554**, 77 (2018).

[13] R. Kabe and C. Adachi, Nature **550**, 384 (2017).

[14] A. Anshul, H. Borkar, P. Singh, P. Pal, S.S. Kushvaha, and A. Kumar, Appl. Phys. Lett. **104**, (2014).

[15] H. Najafov, B. Lee, Q. Zhou, L.C. Feldman, and V. Podzorov, Nat. Mater. **9**, 938 (2010).

[16] D. Beljonne, Z. Shuai, G. Pourtois, and J.L. Bredas, J. Phys. Chem. A **105**, 3899 (2001).

[17] L.B. Niu, L.J. Chen, P. Chen, Y.T. Cui, Y. Zhang, M. Shao, and Y.X. Guan, RSC Adv. **6**, 111421 (2016).

[18] K. Iwano, Y. Shimoi, T. Miyamoto, D. Hata, M. Sotome, N. Kida, S. Horiuchi, and H. Okamoto, Phys. Rev. Lett. **118**, 1 (2017).

[19] A. Pockett, G.E. Eperon, T. Peltola, H.J. Snaith, A. Walker, L.M. Peter, and P.J. Cameron, J. Phys. Chem. C **119**, 3456 (2015).

[20] T. Li, A. Lipatov, H. Lu, H. Lee, J.W. Lee, E. Torun, L. Wirtz, C.B. Eom, J. Íñiguez, A. Sinitskii, and A. Gruverman, Nat. Commun. **9**, (2018).

Chapter 5 Tunable Spin-State Bistability in a Spin Crossover Molecular Complex

5.1 Introduction

In the previous chapters, we discussed organic ferroelectric thin film. In this chapter, we study organic magnetic thin films, in particular, an organic spin crossover (SCO) molecular complex. To investigate the potential of fabricating heterojunctions with the organic magnetic material and the previously discussed ferroelectric material, the interface effect on the magnetic properties of the SCO complex needs to be examined. In this chapter, the spin transition process of a certain SCO complex on the substrates is discussed.

This chapter is reproduced from [Xuanyuan Jiang et al 2019 J. Phys.: Condens. Matter **31** 315401], with the permission of IOP Publishing.

In SCO molecular materials, transition metal centers exhibit spin-state transitions that are driven by entropy and structural changes.[1–5] These SCO transitions, although molecular in origin,[3] become cooperative when the molecules are coupled in a solid, yielding phase-transition-like changes of spin states and even hysteresis in the SCO transition in thermal cycles [as schematically indicated in Fig 5.1.1 (a)], due to the intrinsic coupling of spin state and structure.[2] Various external stimuli can trigger SCO transitions by perturbing either the structure (pressure[2,5,6]) or the electronic states (light,[7–13] charge injection and electromagnetic field[14–16]). This sensitivity to external stimuli may be exploited to realize molecular switches for next generation information storage and processing applications.[15,17-29]

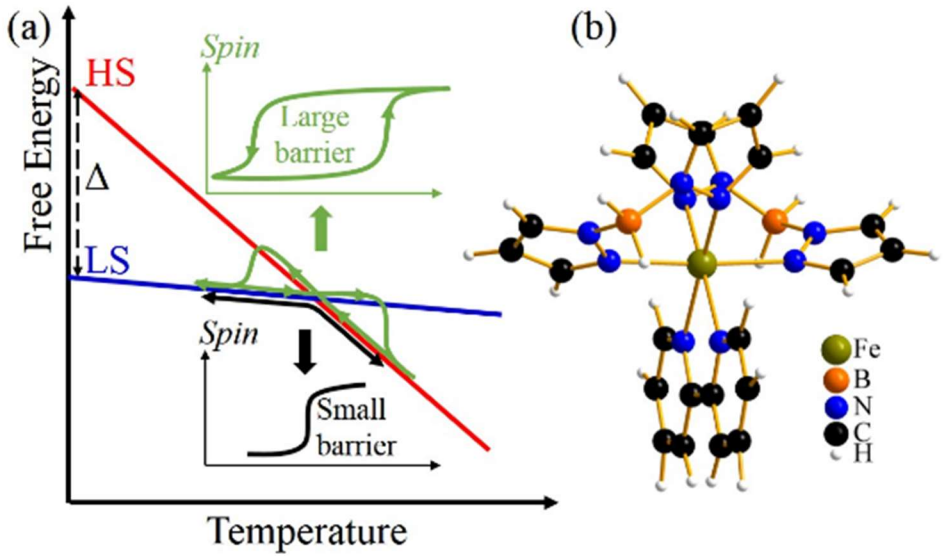

Fig 5.1.1 (a) Schematic energy diagram of the SCO transition, in which the free energy changes with temperature according to entropy. HS state (HS) ↔ LS state transition temperature depends on the enthalpy difference Δ between the spin states. The width of the hysteresis depends on the free-energy barrier between spin states. (b) Molecular structure of [Fe{$H_2B(pz)_2$}$_2$(bipy)].

For widespread applications, one key aspect of the molecular switches is the non-volatile control, which for SCO molecular complexes, requires bistability of the spin states, ideally over a broad temperature range, around room temperature.[11,30,31] Naturally, the coupling of spin state and structure may be employed to achieve this bistability.[2] The challenge is to find the proper enthalpy differences between the spin states [denoted as Δ in Fig 5.1.1 (a)] to place the SCO transition around room temperature and suitable structural differences between the spin states to generate sizable hysteresis.[2,3,5,30] Another route to achieving these goals is to make use of perturbation caused by interactions at a substrate-film interface, because 1) the electronic and structural couplings at the interface may change the enthalpy difference of the spin states (Δ) which changes the SCO transition

temperatures; 2) the modification of the energy barrier between the spin states, by the interface, can tune the width of the hysteresis loop.[29,31-34] In this regard, the spin state of thin-film [Fe{$H_2B(pz)_2$}$_2$(bipy)], a Fe(II) molecular SCO complex, exhibits remarkable tunability, where $H_2B(pz)_2$ = bis(hydrido)bis(1*H*-pyrazol-1-yl)borate, bipy = 2,2'-bipyridine, as shown in Fig 5.1.1 (b). It has already been established that oxide substrates like SiO_2,[35] Al_2O_3,[35] $NiCo_2O_4$,[16] and $La_{0.67}Sr_{0.33}MnO_3$(001) (LSMO)[16] tends to lock very thin [Fe{$H_2B(pz)_2$}$_2$(bipy)] molecular films (< 40 nm) in a largely low-spin (LS) state, to temperatures well above the thermal SCO transition temperature, where the high-spin (HS) state would be generally favored. A comparison of different measurements of the spin-state occupancy suggests that a significant shift of the transition temperature is indeed possible.[36] On the other hand, the effect of the interface on the spin-state bistability, which is caused by the energy barrier between the spin states, has not been fully investigated.

Here we focus on the molecular complex [Fe{$H_2B(pz)_2$}$_2$(bipy)],[37,38] which is among the few SCO molecules that can be evaporated in vacuum without decomposition.[9,16,29,35-41] This molecule exhibits a non-hysteretic transition between a high-temperature HS state and a low-temperature LS state at $T_{1/2}$=157 K in bulk.[29,36-40] The HS and the LS states of the Fe(II) complex correspond to electronic configurations of $t_{2g}^4e_g^2$ (S=2) and $t_{2g}^6e_g^0$ (S=0) respectively, where e_g and t_{2g} are the Fe 3d states split due to the ligand field. We found that the [Fe{$H_2B(pz)_2$}$_2$(bipy)] films, hundreds of nm (300 nm, 900 nm) thick, surprisingly exhibit spin-state hysteresis in thermal cycles around the bulk SCO transition temperature, which suggests bistability.

5.2 Methods

The 300 nm and 900 nm polycrystalline [Fe{$H_2B(pz)_2$}$_2$(bipy)] films were deposited on 5×5 mm^2 Al_2O_3 substrates (at 300 K) using physical vapor deposition in high vacuum (1.0×10^{-7} Torr), with a growth rate of 0.1 Å/s. The temperature dependent (cooling, 2 K/min) x-ray (500 Hz, 80 ps pulse, 1.033 Å) diffraction was carried out at the beamline 14ID-B in the Advanced Photon Source at the Argonne National Lab. The X-ray powder diffraction patterns were measured using a two-dimensional Rayonix MX340-HS detector 40 cm away from the sample and perpendicular to the incident x-ray on a 20×20 μm^2 sample spot for a period of 5 minutes for every temperature. The x-ray damage on [Fe{$H_2B(pz)_2$}$_2$(bipy)] films was checked before the temperature-dependent x-ray diffraction, which showed neither structure change nor material loss after 1.0×10^5 x-ray shots. The temperature of the samples was controlled using a Cryostream system and was calibrated using the lattice constants of the substrates obtained from the experimental diffraction angles.

Temperature dependence of the [Fe{$H_2B(pz)_2$}$_2$(bipy)] magnetic susceptibility (an indicator of spin state) was measured using a superconducting quantum interference device (SQUID) magnetometer.

5.3 Interface effects

The temperature dependence of magnetic susceptibility for two different [Fe{$H_2B(pz)_2$}$_2$(bipy)] films are compared with that of the powder in Fig. 5.3.1. Unlike the powder form, which shows minimum hysteresis as seen in Fig. 5.3.1 and reported elsewhere,[37-40] both [Fe{$H_2B(pz)_2$}$_2$(bipy)] films thicknesses on Al_2O_3 exhibit more prominent hysteresis of the SCO transition. For the 900-nm thick [Fe{$H_2B(pz)_2$}$_2$(bipy)] film, $T_{1/2}$ equals 152 K in cooling and 157 K in warming processes, respectively. Thus

$\Delta T_{1/2} = T_{1/2}^{warm} - T_{1/2}^{cool}$= 5 K. The temperature dependence of the spin-state occupancy (or magnetic susceptibility) of the 300-nm film deviates more significantly from the bulk behavior. As shown in Fig. 5.3.1 (c), the hysteresis measured using magnetometry shows $\Delta T_{1/2} = T_{1/2}^{warm} - T_{1/2}^{cool}$ = 15 K in the 300 nm film, which is three times $\Delta T_{1/2}$ in the 900 nm film. The differences in the extent of the hysteresis, $\Delta T_{1/2}$, suggest that the average energy barrier between the HS and LS states is larger in the 300 nm films than that in the 900 nm films.

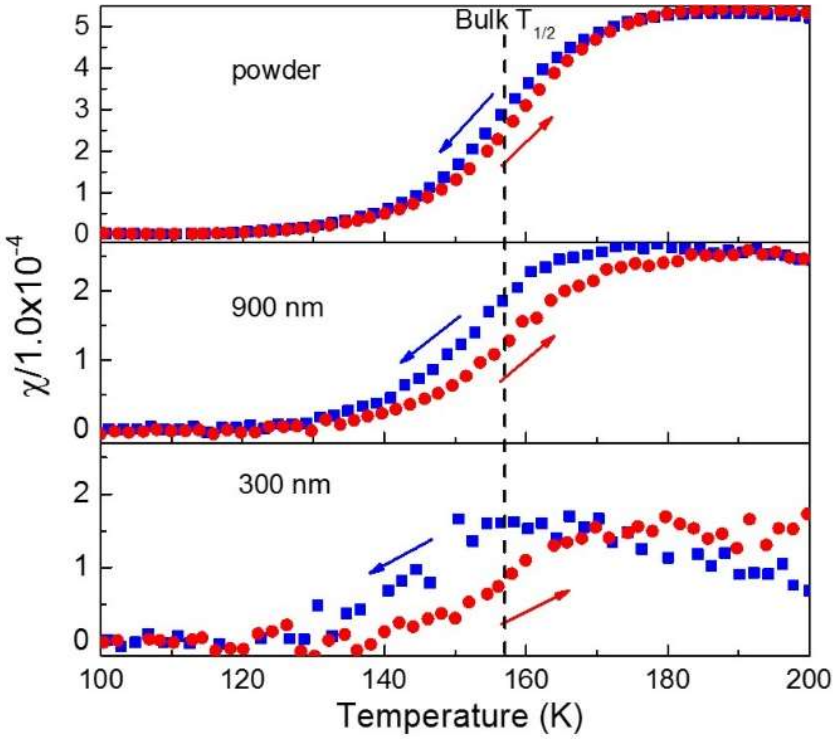

Fig. 5.3.1 Magnetic susceptibility (χ) of (a) powder (b) 900 nm and (c) 300 nm [Fe{$H_2B(pz)_2$}$_2$(bipy)] films, on Al_2O_3, in thermal cycles plotted as scatters dots.

To further probe the transition between the spin states in the 300 nm films, we carried out temperature-dependent X-ray diffraction measurements. The structures of [Fe{$H_2B(pz)_2$}$_2$(bipy)] in bulk are monoclinic with space group $C2/c$ for both the HS and

the LS states.[38] On the other hand, previous work shows that the lattice constants of the HS state (at 300 K) and that of the LS state (at 140 K) differ by about 1.5% which is much larger than what is expected from thermal expansion.[38] This significant difference in lattice constants can be employed to probe the spin state occupancies using x-ray diffraction.

Fig. 5.3.2 (a) shows a typical two-dimensional x-ray powder diffraction pattern. Integrating the azimuthal angle, one gets the powder diffraction intensity as a function of 2θ (diffraction spectrum), which is consistent with the C2/c structure. Fig. 5.3.2 (b) shows the profile near the ($\bar{1}\bar{1}1$) Bragg diffraction peak of the 300 nm thick [Fe{$H_2B(pz)_2$}$_2$(bipy)] film at 125 and 255 K. The diffraction profile at 125 K clearly has a main peak and a shoulder of a similar width at larger 2θ, so the diffraction profile can be fit using two Gaussian functions, as shown by the dashed lines. The centers of the main peak and the shoulder in Fig. 5.3.2 (b) differ by about 1.4%, suggesting that the main peak corresponds to the HS state and the shoulder corresponds to the LS state. [3,38]

Fig. 5.3.2 (c) shows the evolution of the ($\bar{1}\bar{1}1$) diffraction profile when the 300 nm film sample is cooled; the asymmetric broadening of the peaks at low temperature comes from the enhancement of the LS state. By fitting the diffraction profile with the two components, we found that the main diffraction peak shifts towards a higher-angle when the temperature is lowered, as indicated by the line in Fig. 5.3.2 (c), consistent with a lattice constant with linear contraction behavior with a coefficient 1.3×10^{-6} K^{-1}. The ratio between the intensity (area) of the shoulder peak (LS) and that of the main peak (HS) grows upon cooling, as shown in Fig. 5.3.2 (d).

Hence, in the 300 nm film, coexistence of spin state occupancy which indicates bistability, was directly observed using x-ray diffraction, in line with the hysteretic

behavior in the magnetic susceptibility [Fig. 5.3.1 (b)]. Furthermore, the bistability of spin states in the 300-nm film appears to occur at the crystallite level. As shown in Fig. 5.3.2 (b), the widths of the main peak (HS) and the shoulder peak (LS) are similar and insensitive to temperature, indicating that the size of the crystallites for both spin states are similar (about 100 nm).[42] Therefore, the crystallites, as the unit of diffraction, are in either the HS or the LS state. They are spin-state domains.

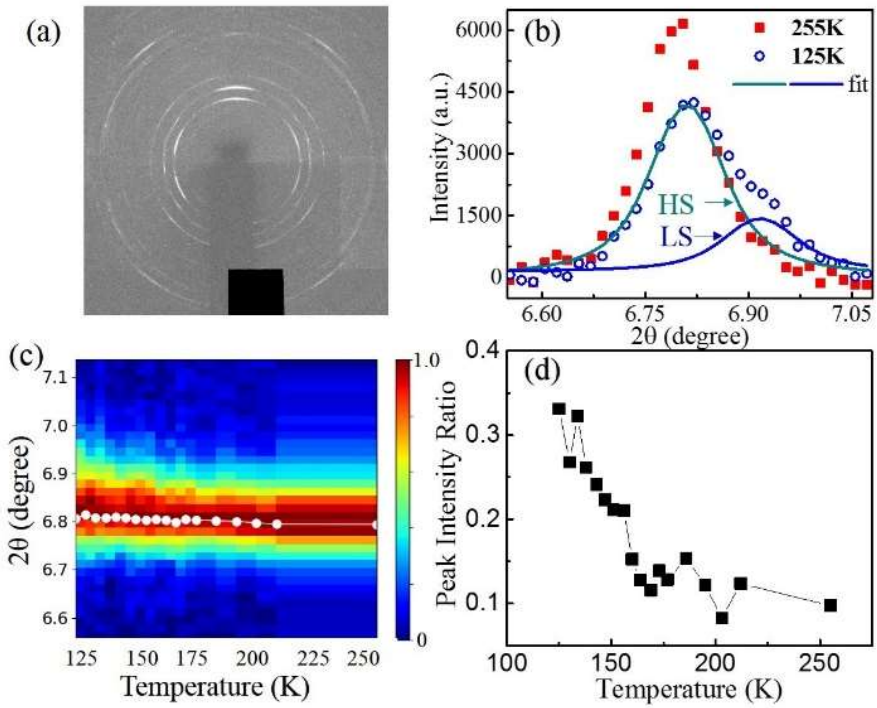

Fig. 5.3.2 (a) Typical powder x-ray diffraction pattern of [Fe{$H_2B(pz)_2$}$_2$(bipy)] films, on Al_2O_3, measured using a two-dimensional detector. The rings show polycrystalline nature of the films. (b)-(d) includes data of a 300 nm film. (b) Diffraction profiles near the $(\bar{1}\bar{1}1)$ Bragg peak; the 125 K profile is fit using a main peak (HS) and a shoulder peak (LS). (c) Diffraction profiles plotted as a two-dimensional image around the $(\bar{1}\bar{1}1)$ Bragg peaks. (d) The intensity ratio between the shoulder (LS) and the main peak (HS) as a function of temperature.

In contrast, the coexistence of both HS and LS spin states was less obvious in the x-ray diffraction of the 900 nm films. Fig. 5.3.3 (a) shows the diffraction spectra near the $(\bar{1}\bar{1}1)$ Bragg peaks of the 900 nm film, in which the size of the crystallites is also about 100 nm according to the peak width.[42] The shape of the 125 K spectrum resembles that taken at 255 K. As shown in Fig. 5.3.3 (b), the evolution of the $(\bar{1}\bar{1}1)$ diffraction profile, as observed during cooling, behaves more like a peak shift due to a lattice constant change, instead of the appearance of an additional peak. Yet the effects seen are non-linear, with the shift of $(\bar{1}\bar{1}1)$ diffraction profile, toward the higher-angles, occurring faster at lower temperatures.

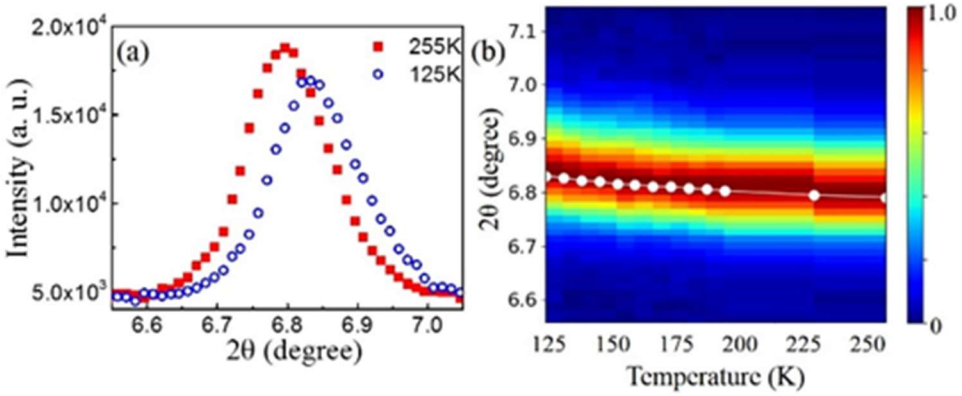

Fig. 5.3.3 X-ray diffraction of a 900 nm thick [Fe{$H_2B(pz)_2$}$_2$(bipy)] film, on Al_2O_3. (a) Diffraction profiles near the $(\bar{1}\bar{1}1)$ Bragg peak at 125 K and 255 K. (b) Diffraction profiles plotted as a two-dimensional image around the $(\bar{1}\bar{1}1)$ Bragg peaks.

The thickness dependence of the SCO transition in the [Fe{$H_2B(pz)_2$}$_2$(bipy)] films on Al_2O_3, suggests that different parts of the films behave differently. If the films are divided into three parts: near substrate, interior, and near surface, the near-substrate part most likely contributes to the hysteretic behavior of the SCO transition the most, because

it is known that the modification of the energy barrier between the spin states of the molecules by the interface can tune the width of the hysteresis loop.[29,31-34] For the [Fe{$H_2B(pz)_2$}$_2$(bipy)]/Al_2O_3 interface, in particular, the LS state of very thin films (< 40 nm) can be locked to temperatures well above the bulk SCO transition temperature, indicating a significant interaction at the substrate/film interface.

5.4 Conclusions

In conclusion, the bistability of the spin states and the spin state hysteresis have been observed in the films of hundreds of nanometers in thickness, indicating tunability of the energy barrier between the spin states in [Fe{$H_2B(pz)_2$}$_2$(bipy)]. The thickness dependence of the hysteresis and the fact that the size of the crystallites are similar in these films, indicate that this effect comes from the [Fe{$H_2B(pz)_2$}$_2$(bipy)]/Al_2O_3 interface.[33,48] Microscopically, the effect of the interface appears to cause the SCO transition collectively at the crystallite level, which enhances the barrier between the spin states and generates hysteresis and bistability in [Fe{$H_2B(pz)_2$}$_2$(bipy)]. The thickness dependence of the hysteresis in spin state also points to a possibility that the temperature range of the bistability can be broadened, perhaps to include room temperature, although this may require a SCO complex different from [Fe{$H_2B(pz)_2$}$_2$(bipy)].

5.5 References

[1] P. Gütlich and H. A. Goodwin, Eds., *Spin Crossover in Transition Metal Compounds I*, Springer-Verlag, Berlin, Heidelberg, 2004.

[2] P. Gütlich, Y. Garcia and H. A. Goodwin, *Chem. Soc. Rev.*, 2000, **29**, 419–427.

[3] M. A. Halcrow, *Chem. Soc. Rev.*, 2011, **40**, 4119–4142.

[4] P. Gütlich and H. A. Goodwin, Eds., *Spin Crossover in Transition Metal Compounds II*, Springer-Verlag, Berlin, Heidelberg, 2004.

[5] M. Shatruk, H. Phan, B. A. Chrisostomo and A. Suleimenova, *Coord. Chem. Rev.*, 2015, 289–290, 62–73.

[6] A. Galet, A. B. Gaspar, G. Agusti, M. C. Muñoz, G. Levchenko and J. A. Real, *Eur. J. Inorg. Chem.*, 2006, **18**, 3571–3573.

[7] N. Matsumoto, T. Sato, S. Hashimoto, M. Kojima and S. Iijima, *J. Phys. Conf. Ser.*, 2009, **148**, 012029.

[8] S. Ohkoshi, K. Imoto, Y. Tsunobuchi, S. Takano and H. Tokoro, *Nat. Chem.*, 2011, **3**, 564–569.

[9] B. Warner, J. C. Oberg, T. G. Gill, F. El Hallak, C. F. Hirjibehedin, M. Serri, S. Heutz, M.-A. Arrio, P. Sainctavit, M. Mannini, G. Poneti, R. Sessoli and P. Rosa, *J. Phys. Chem. Lett.*, 2013, **4**, 1546–1552.

[10] G. Auböck and M. Chergui, Nat. Chem., 2015, 7, 629–633.

[11] E. Freysz, S. Montant, S. Létard and J.-F. Létard, *Chem. Phys. Lett.*, 2004, **394**, 318–323.

[12] S. Bonhommeau, G. Molnár, A. Galet, A. Zwick, J.-A. Jeal, J. J. McGarvey and A. Bousseksou, *Angew. Chemie*, 2005, **44**, 4069–4073.

[13] S. Cobo, D. Ostrovskii, S. Bonhommeau, L. Vendier, G. Molnár, L. Salmon, K. Tanaka and A. Bousseksou, *J. Am. Chem. Soc.*, 2008, **130**, 9019–9024.

[14] T. Miyamachi, M. Gruber, V. Davesne, M. Bowen, S. Boukari, L. Joly, F. Scheurer, G. Rogez, T. K. Yamada, P. Ohresser, E. Beaurepaire and W. Wulfhekel, *Nat. Commun.*, 2012, **3**, 938.

[15] T. G. Gopakumar, F. Matino, H. Naggert, A. Bannwarth, F. Tuczek and R. Berndt, *Angew. Chemie - Int. Ed.*, 2012, **51**, 6262–6266.

[16] X. Zhang, A. T. N. Diaye, X. Jiang, X. Zhang, Y. Yin, X. Chen, X. Hong, X. Xu and P. A. Dowben, *Chem. Commun.*, 2018, **54**, 944–947.

[17] G. Molnár, S. Rat, L. Salmon, W. Nicolazzi and A. Bousseksou, *Adv. Mater.*, 2018, **30**, 17003862.

[18] A. Cornia and P. Seneor, *Nat. Mater.* 2017, **16**, 505.

[19] D. Aravena and E. Ruiz, *J. Am. Chem. Soc.* 2012, **134**, 777.

[20] W. Kuch and M. J. Bernien, *J. Phys. Condens. Matter* 2017, **29**, 023001.

[21] E. Ludwig, H. Naggert, M. Kalläne, S. Rohlf, E. Kröger, A. Bannwarth, A. Quer, K. Rossnagel, L. Kipp, and F. Tuczek, *Angew. Chem., Int. Ed.* 2014, **53**, 3019.

[22] T. Mahfoud, G. Molnar, S. Bonhommeau, S. Cobo, L. Salmon, P. Demont, H. Tokoro, S.-I. Ohkoshi, K. Boukheddade, and A. Bousseksou, *J. Am. Chem. Soc.* 2009, **131**, 15049.

[23] T. Mahfoud, G. Molnar, S. Cobo, L. Salmon, C. Thibault, C. Vieu, P. Demont, and A. Bousseksou, *Appl. Phys. Lett.* 2011, **99**, 053307.

[24] T. Miyamachi, M. Gruber, V. Davesne, M. Bowen, S. Boukari, L. Joly, F. Scheurer, G. Rogez, T. K. Yamada, P. Ohresser, E. Beaurepaire, and W. Wulfhekel, Nat. Commun. 2012, **3**, 938.

[25] F. Prins, M. Monrabal-Capilla, E. A. Osorio, E. Coronado, and H. S. van der, Zant, *J. Adv. Mater.* 2011, **23**, 1545.

[26] A. Rotaru, I. Y. A. Gural'skiy, G. Molnar, L. Salmon, P. Demont, and A. Bousseksou, Chem. Commun. 2012, **48**, 4163.

[27] A. Rotaru, J. Dugay, R. P. Tan, I. A. Gural'skiy, L. Salmon, P. Demont, J. Carrey, G. Molnar, M. Respaud, and A. Bousseksou, Adv. Mater. 2013, **25**, 1745

[28] E. Ruiz, Phys. Chem. Chem. Phys. 2014, **16**, 14

[29] A. Pronschinske, Y. Chen, G. F. Lewis, D. A. Shultz, A. Calzolari, M. B. Nardelli and D. B. Dougherty, *Nano Lett.*, 2013, **13**, 1429–1434.

[30] P. Guionneau, F. Le Gac, S. Lakhoufi, A. Kaiba, D. Chasseau, J. F. Létard, P. Négrier, D. Mondieig, J. A. K. Howard and J. M. Léger, *J. Phys. Condens. Matter*, 2007, **19**, 326211.

[31] G. Zoppellaro, J. Tuček, J. Ugolotti, C. Aparicio, O. Malina, K. Čépe and R. Zbořil, *Chem. Mater.*, 2017, **29**, 8875–8883.

[32] M. Gruber, V. Davesne, M. Bowen, S. Boukari, E. Beaurepaire, W. Wulfhekel and T. Miyamachi, *Phys. Rev. B - Condens. Matter Mater. Phys.*, 2014, **89**, 195415.

[33] G. Félix, W. Nicolazzi, L. Salmon, G. Molnár, M. Perrier, G. Maurin, J. Larionova, J. Long, Y. Guari and A. Bousseksou, *Phys. Rev. Lett.*, 2013, **110**, 235701.

[34] Y. Raza, F. Volatron, S. Moldovan, O. Ersen, V. Huc, C. Martini, F. Brisset, A. Gloter, O. Stéphan, A. Bousseksou, L. Catala and T. Mallah, *Chem. Commun.*, 2011, **47**, 11501–11503.

[35] X. Zhang, P. S. Costa, J. Hooper, D. P. Miller, A. T. N'Diaye, S. Beniwal, X. Jiang, Y. Yin, P. Rosa, L. Routaboul, M. Gonidec, L. Poggini, P. Braunstein, B. Doudin, X. Xu, A. Enders, E. Zurek and P. A. Dowben, *Adv. Mater.*, 2017, **29**, 1702257.

[36] X. Zhang, S. Mu, G. Chastanet, N. Daro, T. Palamarciuc, P. Rosa, J. F. Létard, J. Liu, G. E. Sterbinsky, D. A. Arena, C. Etrillard, B. Kundys, B. Doudin and P. A. Dowben, *J. Phys. Chem. C*, 2015, **119**, 16293–16302.

[37] T. Palamarciuc, J. C. Oberg, F. El Hallak, C. F. Hirjibehedin, M. Serri, S. Heutz, J. F. Létard and P. Rosa, *J. Mater. Chem.*, 2012, **22**, 9690–9695.

[38] J. A. Real, M. C. Muñoz, J. Faus and X. Solans, *Inorg. Chem.*, 1997, **36**, 3008–3013.

[39] X. Zhang, T. Palamarciuc, P. Rosa, J. F. Létard, B. Doudin, Z. Zhang, J. Wang and P. A. Dowben, *J. Phys. Chem. C*, 2012, **116**, 23291–23296.

[40] N. Moliner, L. Salmon, L. Capes, M. C. Muñoz, J. F. Létard, A. Bousseksou, J. P. Tuchagues, J. J. McGarvey, A. C. Dennis, M. Castro, R. Burriel and J. A. Real, *J. Phys. Chem. B*, 2002, **106**, 4276–4283.

[41] S. Beniwal, X. Zhang, S. Mu, A. Naim, P. Rosa, G. Chastanet, J. F. Létard, J. Liu, G. E. Sterbinsky, D. A. Arena, P. A. Dowben and A. Enders, *J. Phys. Condens. Matter*, 2016, **28**, 206002.

[42] B. D. Cullity, *Elements of X-Ray DIFFRACTION*, Addison-Wesley, 1956.

[43] C. Wäckerlin, F. Donati, A. Singha, R. Baltic, S. Decurtins, S. X. Liu, S. Rusponi and J. Dreiser, *J. Phys. Chem. C*, 2018, **122**, 8202–8208.

[44] A. Pronschinske, R. C. Bruce, G. Lewis, Y. Chen, A. Calzolari, M. Buongiorno-Nardelli, D. A. Shultz, W. You and D. B. Dougherty, *Chem. Commun.*, 2013, **49**, 10446–10452.

[45] G. Hao, A. Mosey, X. Jiang, A. J. Yost, K. R. Sapkota, G. T. Wang, X. Zhang, J. Zhang, A. T. N'Diaye, R. Cheng, X. Xu and P. A. Dowben, *Appl. Phys. Lett.*, 2019, **114**, 032901.

[46] X. Zhang, T. Palamarciuc, J.-F. Létard, P. Rosa, E. V. Lozada, F. Torres, L. G. Rosa, B. Doudin and P. A. Dowben, *Chem. Commun.*, 2014, **50**, 2255.

[47] R. Franz and G. Wiedemann, *Ann. der Phys. und Chemie*, 1853, **165**, 497–531.

[48] J. Larionova, L. Salmon, Y. Guari, A. Tokarev, K. Molvinger, G. Molnár and A. Bousseksou, *Angew. Chemie - Int. Ed.*, 2008, **47**, 8236–8240.

Chapter 6 Nonvolatile spin-state switching in the organic heterostructure

6.1 Introduction

In previous chapters, we have studied the ferroelectricity in Croconic Acid (CA) and magnetism in spin crossover (SCO) complex [Fe{$H_2B(pz)_2$}$_2$(bipy)] (BIPY). A CA/BIPY based organic multiferroic memory device, where the information can be written by electric field and read through magnetic or transport properties, can be expected. In this chapter, we combine these two materials in a thin film transport junction and realize the polarization-controlled spin transition and the corresponding charge transport.

This chapter is reproduced from [Appl. Phys. Lett. **114**, 032901 (2019)], with the permission of AIP Publishing.

6.2 Methods

The 20 nm BIPY thin films were deposited on top of 200 nm thick CA thin films, which were deposited on silicon oxide substrates with preprinted interdigitated gold electrodes. The application of poling voltage and the measurement of resistance across the junction are both conducted via a source meter Keithley 236. And all the measurements are performed in air at the room temperature.

6.3 Polarization controlled spin transition

The free energy profile of the high spin (HS) and low spin (LS) states in terms of temperature in BIPY is described in chapter 5. The spin transition temperature can be modified by the energy difference between these two spin states[1]. It has been shown that the modification can be realized by enhancing the effect of magnetoelectric coupling in the BIPY molecules through the interface effect[2]. The uncompensated charges distributed at

the interface of BIPY and substrate generate an interfacial electric field. According to the calculation in Xin Zhang's paper[2], the HS and LS states have different dipole moments. The interaction between the field and the molecular dipole moments would have different impacts on the free energy of HS and LS states and tend to stabilize one of them at a certain temperature.

As a result, the energy difference between the two spin states would be tuned. Depending on the direction of the interfacial electric field with respect to the molecular moments, parallel or antiparallel, the energy difference can be either decreased or increased, leading to left or right shifting of the spin transition temperature, as shown in Fig. 6.3.1.

The interfacial electric field can be introduced by ferroelectric materials. Upon polarization reversal, the direction of the interfacial field can be flipped[3,4]. In other word, the parallel and antiparallel configuration, and thus the shifting of the transition temperature, can be controlled by the polarization of the ferroelectric layer.

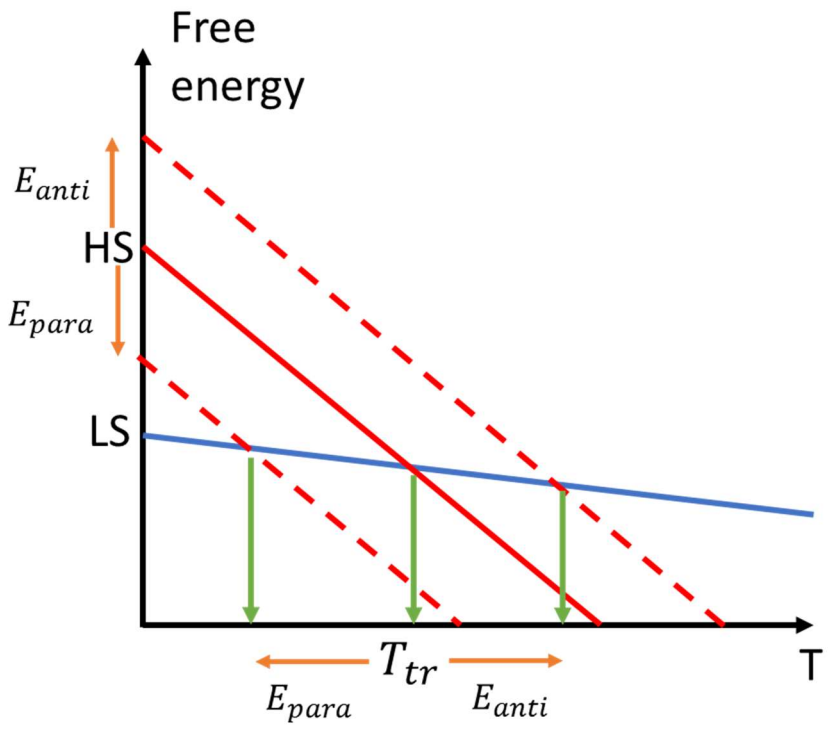

Fig. 6.3.1 Schematic diagram of electric-field-shifting spin transition temperature T_{tr}.

6.4 Nonvolatile resistive switching

The in-plane device structure is sketched in Fig. 6.4.1 (b). The 200 nm CA was grown on the interdigital bottom electrode, and 20 nm BIPY was deposited afterwards. The gap between the two Au electrodes was measured through scanning electron microscope (SEM), which is around 262 nm (Fig. 6.4.1 (a)). The height of the bottom electrode is around 60 nm. Since the CA layer grown in this device is quite rough[3,11], the gap between electrodes is not fully covered by CA and partially filled by BIPY (Fig. 6.4.1 (b)).

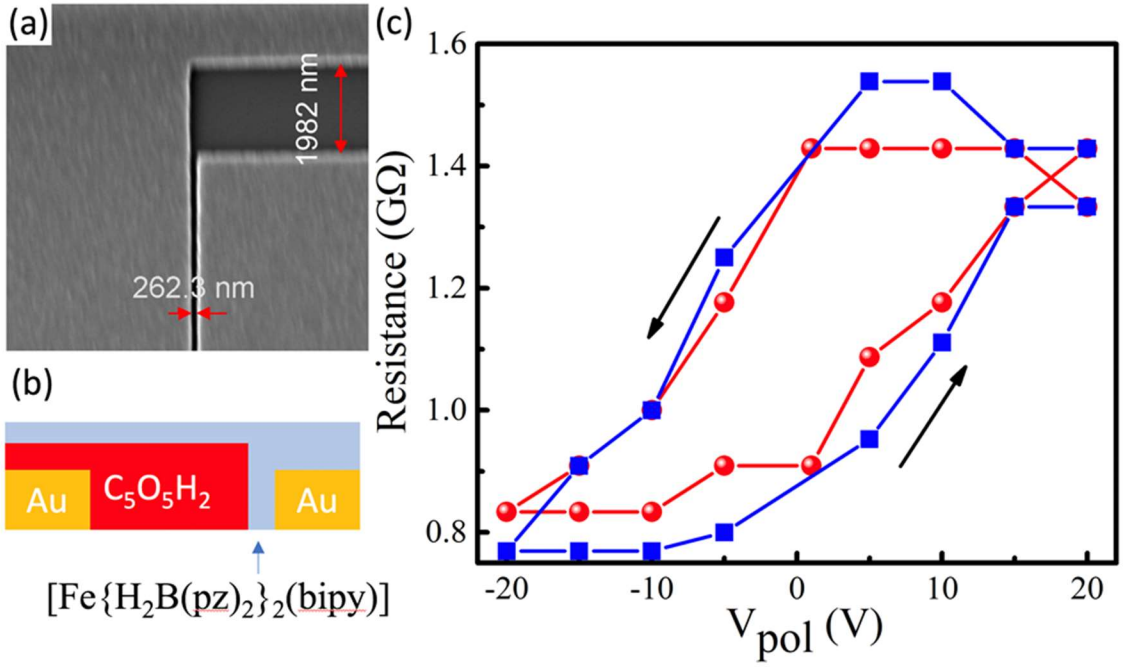

Fig. 6.4.1 (a) The scanning electron microscopy image of the bottom electrodes. (b) The schematic in-plane device structure. (c) Poling voltage dependence of resistance switching (red and blue lines indicate different scans)[5].

The nonvolatile resistance switching is achieved in this in-plane device. By measuring the current flowing through the CA/BIPY junction at 1V, the poling voltage dependent resistance states are recorded[5]. The reproducible switching between high and low resistance states is revealed (Fig. 6.4.1 (c)). The switching field is related to the coercive field in CA, which proves that the resistance switching is determined by the polarization reversal in CA thin film.

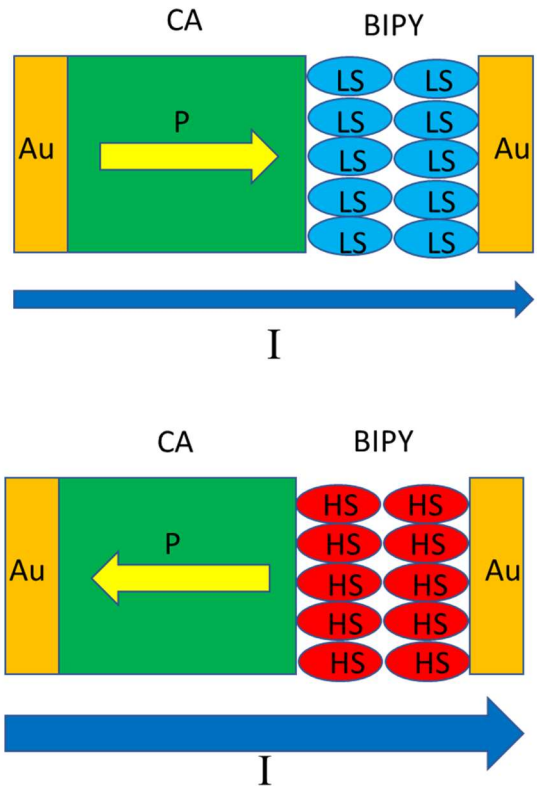

Fig. 6.4.2 Schematic diagram of resistive switching in the CA/BIPY heterojunction.

The nonvolatile resistive switching in this organic heterojunction can be explained by the superposition of polarization reversal induced spin state transition and difference in conductivity of the two spin states (as sketched in Fig. 6.4.2). In this in-plane device structure, the CA and BIPY molecules are arranged in series between the electrodes (Fig. 6.4.2). When the polarization of CA is switched by the poling voltage, the interfacial interaction will introduce the spin state transition. Due to different electronic structures of the two spin states, the conductivity of BIPY is also changed[6]. In a word, the polarization induced selection of spin states affects the magnitude of current through the heterojunction. When the polarization in CA points to the right, the BIPY molecules are locked in LS state

with low conductivity, and the current is small. And in the opposite case, the BIPY molecules prefer HS state with larger conductivity and large current.

6.5 Conclusion

By fabricating nanosized in-plane electronic device, switching between the high and low resistance states is obtained upon the flip of polarization in ferroelectric material. This study shows the potential of building a pure organic multiferroic memory device, which may substitute or complement the current inorganic ferromagnetic or ferroelectric electronics.

6.6 Reference

[1] X. Jiang, G. Hao, X. Wang, A. Mosey, X. Zhang, L. Yu, A.J. Yost, A.D. DiChiara, A.T. N'Diaye, X. Cheng, J. Zhang, R. Cheng, X. Xu, and P.A. Dowben, J. Phys. Condens. Matter **31**, (2019).

[2] X. Zhang, P.S. Costa, J. Hooper, D.P. Miller, A.T. N'Diaye, S. Beniwal, X. Jiang, Y. Yin, P. Rosa, L. Routaboul, M. Gonidec, L. Poggini, P. Braunstein, B. Doudin, X. Xu, A. Enders, E. Zurek, and P.A. Dowben, Adv. Mater. **29**, (2017).

[3] X. Jiang, H. Lu, Y. Yin, X. Zhang, X. Wang, L. Yu, Z. Ahmadi, P.S. Costa, A.D. Dichiara, X. Cheng, A. Gruverman, A. Enders, and X. Xu, Appl. Phys. Lett. **109**, (2016).

[4] R. Tadros-Morgane, T. Steinmetz, R. Florange, and H. Kliem, Ferroelectrics **304**, 47 (2004).

[5] G. Hao, A. Mosey, X. Jiang, A.J. Yost, K.R. Sapkota, G.T. Wang, X. Zhang, J. Zhang, A.T. N'Diaye, R. Cheng, X. Xu, and P.A. Dowben, Appl. Phys. Lett. **114**, (2019).

[6] X. Zhang, T. Palamarciuc, J.F. Létard, P. Rosa, E.V. Lozada, F. Torres, L.G. Rosa, B. Doudin, and P.A. Dowben, Chem. Commun. **50**, 2255 (2014).

[7] X. Zhang, S. Mu, G. Chastanet, N. Daro, T. Palamarciuc, P. Rosa, J.F. Létard, J. Liu, G.E. Sterbinsky, D.A. Arena, C. Etrillard, B. Kundys, B. Doudin, and P.A. Dowben, J. Phys. Chem. C **119**, 16293 (2015).

[8] X. Zhang, A.T. N'Diaye, X. Jiang, X. Zhang, Y. Yin, X. Chen, X. Hong, X. Xu, and P.A. Dowben, Chem. Commun. **54**, (2018).

[9] D. Di Sante, A. Stroppa, and S. Picozzi, Phys. Chem. Chem. Phys. **14**, 14673 (2012).

[10] S. Horiuchi, Y. Tokunaga, G. Giovannetti, S. Picozzi, H. Itoh, R. Shimano, R. Kumai, and Y. Tokura, Nature **463**, 789 (2010).

[11] Y. Yuan, X. Jiang, S. Poddar, X. Xu, CrysEngComm. (2019).

Chapter 7 Summary

This dissertation mainly focuses on the study of thin films based on organic materials, ferroelectric CA and spin crossover molecule BIPY. The growth conditions and characterizations of various properties in the two materials were examined.

CA has small coercive field and large spontaneous polarization, of which the out-of-plane projection can be retained even in thin films. These advantages make it a promising material for information writing.

Paramagnetic HS and diamagnetic LS states co-exist in BIPY and process different conductivities. Transition between the two states can be achieved by many external stimuli. Detection of the magnetic or resistance states in BIPY can serve as readout methods of stored information.

In an in-plane multiferroic electronic device based on CA and BIPY, we have realized both the spin state transition and resistive switching under electric fields. The spin state of BIPY is selected by the polarization of CA. Locking of the spin states can be reflected by the magnetic or electrical response of the device.